Renewable Energy 219 (2023) 118694

Contents lists available at ScienceDirect

Renewable Energy

journal homepage: www.elsevier.com/locate/renene

Turbulence modeling to aid tidal energy resource characterization in the Western Passage, Maine, USA

Mithun Deb [a,*], Zhaoqing Yang [a,c], Taiping Wang [a], Levi Kilcher [b]

[a] Marine and Coastal Research Laboratory, Energy and Environment Directorate, Pacific Northwest National Laboratory, Sequim, WA, 98382, USA
[b] National Renewable Energy Laboratory, Golden, CO, 80401, USA
[c] Department of Civil and Environmental Engineering, University of Washington, Seattle, WA, 98195, USA

ARTICLE INFO

Keywords:
Marine renewable energy
Tidal stream energy
Turbulence
Numerical modeling
Tidal energy converters
Resource characterization

ABSTRACT

Numerical models combined with field measurements are regularly used to characterize tidal energy resources at potential energetic sites. However, most existing works only focus on the tidal hydrodynamic characteristics, and turbulence parameters are often not reported because of the lack of high-quality turbulence measurements and the limitations of numerical models in resolving turbulent eddies. In this study, we used FVCOM – a hydrostatic primitive equation (HPE) model – to characterize the tidal energy resource in the Western Passage, Maine, USA, by taking care of the essential macro-scale turbulence properties. We observed an excellent model performance using the Mellor–Yamada Level 2.5 Turbulence Model; estimating the spatial and vertical distribution of the turbulent kinetic energy and intensity added a new perspective to the site ranking for tidal energy converter (TEC) deployments. In addition, we also examined the role of channel geometry and bathymetry, such as headlands and underwater sills, in enhancing turbulent eddies around potential TEC siting locations. Ultimately, the detailed analysis of the turbulent flow characteristics has changed the site-ranking results and demonstrated that the regional-scale HPE models could be used for the relative understanding of more or less turbulent sites for a refined resource assessment.

1. Introduction

In response to rising concern over global climate change and carbon-free energy generation, marine renewable energy is seeing increasing interest as an alternative source of clean energy [1,2]. Tidal stream energy has advantages over other marine renewable energy sources, such as offshore wind and wave energy, due to the continuous and predictable nature, stability, and ideal locations near coastal communities. During tidal energy resource assessment, various regional-scale 2D/3D numerical modeling frameworks have been used over the years to identify tidal stream hotspots [3–8]. These state-of-the-art ocean models provide essential hydrodynamic properties, such as horizontal and vertical variation of tidal velocity, where the former is used for estimating the undisturbed power density potential throughout the entire area of interest. The mean power density variability across various channel sections or the mean kinetic energy flux available at the exact locations is then used to rank the suitable sites for harnessing tidal power [9].

The International Electrotechnical Commission (IEC) maintains a guidance system for tidal resource assessments, such as IEC Technical Specification (TS) 62600-201 [10], which asks for accurate flow properties to aid the installation of arrays of tidal energy converters (TECs). The requirements vary based on project size, where IEC TS 62600-201 recommends using direct field measurements or hydrodynamic modeling, or both combined, to provide detailed information on flow properties in the location of interest. More specifically, for a small project where the total extracted power is less than 10 MW or 2% of the theoretical power available, the resource characterization and assessment can be performed based on a numerical model without simulating energy extraction or velocity measurements at the turbine locations under undisturbed conditions. And, if the total expected power output at the project site is higher than 10 MW or 2% of the theoretical value, the effect of energy extraction must be simulated in the numerical models and the field measurements should be used to support the model validation. In addition to the variables needed for resource assessment, IEC TS 62600-201 also recommends quantifying turbulence intensity (I_u) and providing turbulence statistics such as turbulent kinetic energy (TKE), Reynolds stresses, and other important properties to help 'Stage-2' assessments [10]. Mainly, designers use these turbulence quantities to test device performance and fatigue loads.

In highly energetic tidal flows, the time and length scale of the turbulent eddies can vary widely based on the along- and across-channel bathymetric properties. To resolve these small-scale structures,

* Corresponding author.
E-mail address: mithun.deb@pnnl.gov (M. Deb).

https://doi.org/10.1016/j.renene.2023.04.100
Received 2 November 2022; Received in revised form 17 April 2023; Accepted 21 April 2023
Available online 26 April 2023

we need computationally expensive methods like large eddy simulation [LES; Spalart [11]], which is still not feasible for implementation when tidal resource assessment in a large domain is considered. A 3D ocean model with Reynolds-Averaged Navier–Stokes (RANS) approach and further assumptions of the flow properties (hydrostatic and Boussinesq approximations) solves hydrostatic primitive equations [e.g.,12, 13] that can be useful for a general 'Stage-1' feasibility study of an area of interest. More specifically, resolving turbulence macro-scale properties using 3D hydrostatic primitive equation (HPE) models can add essential information for 'Stage-1' TEC site characterization. For example, Thyng et al. [14] and Guerra et al. [15] have used HPE models to generate turbulence statistics to assess potential tidal turbine sites within energetic tidal channels at Admiralty Inlet, WA, USA, and Chacao Channel, Chile, respectively.

In this study, we focus on implementing a 3D HPE model — the Finite Volume Community Ocean Model [FVCOM; Chen et al. [13]] in a top-ranked tidal energy site in the US (Western Passage, ME) to demonstrate how the macro-scale turbulence properties can be used to help identify and rank suitable locations for TECs. The Western Passage is an energetic tidal channel between New Brunswick, Canada, and the state of Maine in the United States (Figs. 1a and 2), which is part of a large and complex coastal system — the Passamaquoddy–Cobscook Bay archipelago [16–19]. This archipelago is connected to the Bay of Fundy, which has the largest tidal range in the world [20]. The narrow southern portion of the Western Passage is a top-ranked site for tidal stream energy based on several criteria: available tidal power density, market value, energy price, shipping cost, and transmission distance, in addition to its suitable geological and bathymetric configurations for existing tidal energy technologies [9,21]. The large channel volume flux, in conjunction with the rugged landscape (cliffs and large headlands extending into the bay, Fig. 2), however, generates the Western Hemisphere's largest tidal whirlpool, Old Sow (https://www.bayoffundy.com/about/old-sow-whirlpool/). Old Sow occurs toward the Canadian side of the Western Passage near the southern tip of Deer Island, where most of the flood tide enters from the main channel in the northeast between Campobello and Deer islands. Tidal water from the open ocean initially bifurcates into a tributary (Indian River) and the main channel from the positioning of Indian Island. These two streams meet again before reaching the Western Passage, creating a confluence zone and generating eddies that produce Old Sow and highly turbulent conditions. Past studies [22–26] have shown that, depending on the velocity and momentum ratio of the two streams, a confluence hydrodynamic zone can form immediately within and downstream of stream junctions where complex 3D eddy motions ('wake mode' or 'Helmholtz mode' instabilities) dominate.

The complex flow conditions observed in the Western Passage posited a case for assessing the turbulence variation throughout the entire channel during resource characterization and before proposing the most suitable location for TEC farm deployment. The model chosen for this study, FVCOM, uses a two-equation Mellor–Yamada level 2.5 (MY2.5) turbulent closure scheme [27,28] that resolves turbulence macro-scale (wavelength containing peak turbulent energy) to parameterize the vertical eddy viscosity [13]. The MY2.5 turbulence model has been widely used in different ocean circulation models [29–32] for parameterizing vertical mixing and is considered one of the standard schemes for coastal ocean applications.

The primary objective of this study is to integrate macro-scale turbulent flow properties such as TKE and I_u, among others, in the tidal energy resource characterization and rank suitable locations for TEC arrays. Based on this objective, we first compared the performance of the 3D ocean model against a dense network of field data sets collected from the Western Passage. After conducting an extensive model validation, we ran a month-long simulation consisting of two spring and neap cycles to evaluate the tempo-spatial variability of tidal power density and turbulence properties in the Western Passage. Subsequently, we used the modeled turbulence characteristics to investigate the flow unsteadiness at energetic channel transects. A sensitivity analysis is also developed to show that turbulence production in potential TEC sites near channel confluence and headlands depend significantly on the momentum ratio and local bathymetric features of the main channel and tributaries. Ultimately, with these model results, we tried to understand which specific locations within Western Passage are most promising for TEC siting and if the same modeling framework can be used to compare turbulence between different channels.

2. Methodology

In this study, tidal hydrodynamics and turbulence variables were generated for two purposes: (1) hydrodynamic model validation and (2) a resource assessment for tidal farm development in Western Passage. First, data sets from different tide gauges (e.g., surface elevation, harmonic constituents) were used to calibrate and validate the model following the recommendation of IEC TS 62600-201. Tidal current data sets can provide site-specific details on the magnitude and direction of flow velocity throughout the water column required to estimate annual energy production and kinetic energy flux calculation, which ultimately aid in ranking the resources [8]. We used multiple current profiler data sets from the Western Passage to validate flow predictions from the 3D model. Kilcher [33] collected field data sets of turbulent kinetic energy and intensity from the study site following IEC TS 62600-201 guidelines. We used this publicly available data set to validate our model-generated turbulence statistics. Then, we used the validated model results of turbulence with other flow variables for resource assessment.

2.1. Field data

To define the model grid bathymetry, we obtained publicly available bathymetry data sets from two sources: (1) ETOPO1 1-arc-minute Global Relief Model [34] and (2) Eastern Canada 3 arc-second Bathymetric Digital Elevation Model [35], the highest resolution available during this study for Western Passage. While ETOPO1 1-arc-minute Global Relief Model data is used for the large area of the Bay of Fundy and Gulf of Maine, the Eastern Canada 3 arc-second (~90 m) data set is used explicitly for resolving the complex shallow features in the Western Passage main channel and tributaries. To calibrate the model-predicted water surface elevation, we selected the only National Oceanic and Atmospheric Administration (NOAA) tide gauge available in the study area: Eastport, ME (station id = 8410140), and two XTide stations: Cutler, ME, and Port Greville, NS (https://flaterco.com/xtide/) (Fig. 1a). We also used three historical acoustic Doppler current profiler (ADCP) current data sets: EP0003, EP0004, and J02 (Fig. 2), from locations close to the Western Passage, for further model validation. These stations consist of historical data sets from different periods. More information about these data sets can be found in [9]. As part of a tidal resource assessment study, Kilcher [33] collected various flow and turbulence data sets using vessel and bottom-mounted ADCPs and an acoustic Doppler velocimeter (ADV) from the Western Passage. They conducted this field campaign during April–July 2017, and different instruments were used to measure flow properties at different locations and periods. For example, the ADV mounted on a stable tidal turbulence mooring (STTM) was deployed at 10 m above the bottom (mab) and collected turbulence data from 24–31 May 2017, while the ADCPs collected data for a much longer period (~3 months). These data sets were post-processed using Doppler Oceanography Library for pYthoN (DOLfYN) version 0.11.2 (https://lkilcher.github.io/dolfyn), and shared in a public directory: https://www.osti.gov/dataexplorer/biblio/dataset/1635227. In this study, we have used the tidal turbulence statistics and current data collected in 2017 at the Western Passage, shown as WP in Fig. 2, for model validation.

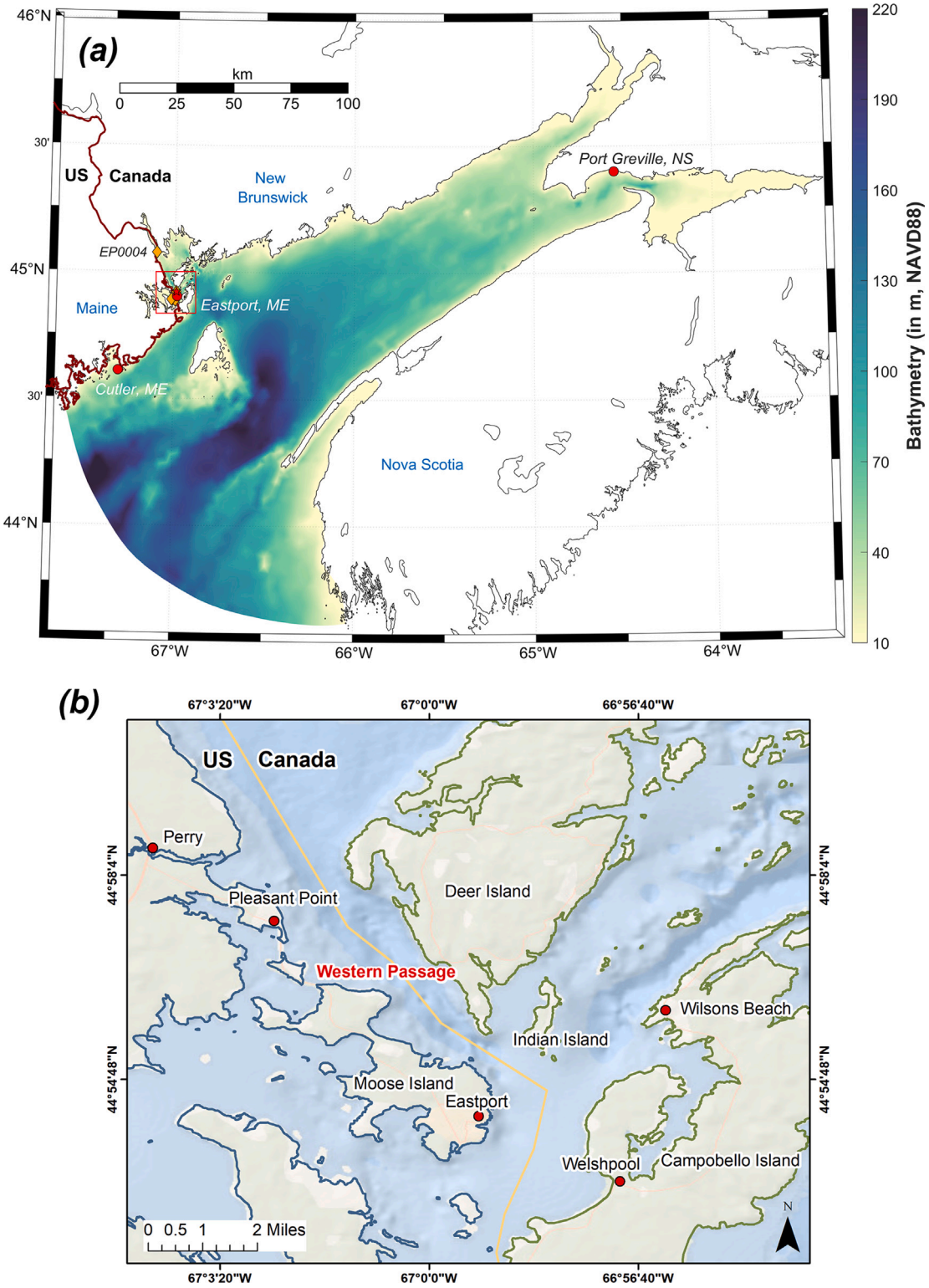

Fig. 1. (a) Unstructured grid model domain and bathymetry (in meters). Red polygon shows the location of the Western Passage in the domain, and red circles and yellow diamonds represent tide and acoustic Doppler current profiler gauges used for model validation, respectively. (b) The Western Passage energetic tidal channel between New Brunswick, Canada, and the state of Maine in the United States.

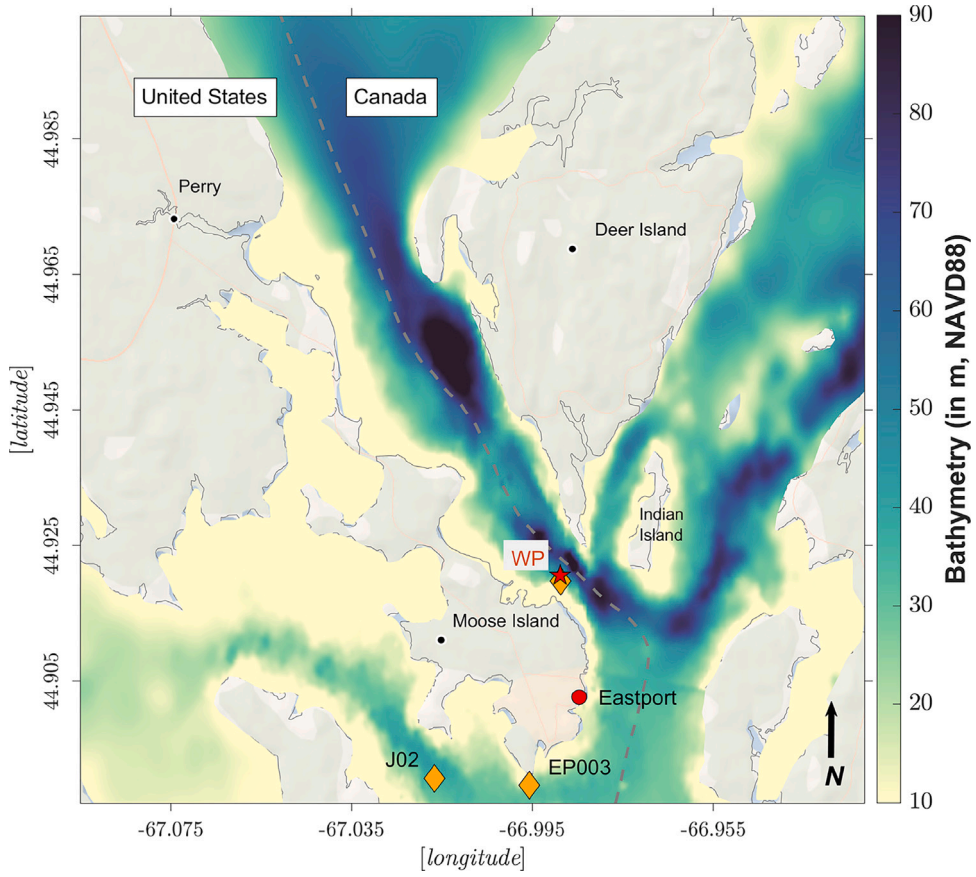

Fig. 2. Model bathymetry (in meters) in the Western Passage, ME, interpolated from NOAA Eastern Canada 3 arc-second digital elevation model (DEM). Red circles and yellow diamonds represent tide and ADCP gauges used for model validation, respectively, and the red star represents the STTM location.

2.2. Numerical model

We used the unstructured-grid, finite-volume, community ocean model FVCOM [13] in this study to simulate tidal hydrodynamics and flow structures. FVCOM is a 3D ocean model that solves primitive governing equations (RANS) for momentum, temperature, salinity, and density. It has been used in many estuarine and coastal studies consisting of complex topo-bathymetry, inter-tidal wetting and drying, and irregular coastline [e.g.,8,36,37]. Some of the essential equations in FVCOM for mean and turbulent flow are given briefly in the following section.

2.2.1. Governing equations

The incompressible, u-momentum equation in FVCOM is given as

$$\frac{\partial u}{\partial t} + \mathbf{u}\cdot\nabla u - fv = -\frac{1}{\rho_0}\frac{\partial P}{\partial x} + \frac{\partial}{\partial z}\left(K_m\frac{\partial u}{\partial z}\right) + F_u \tag{1}$$

where, $\mathbf{u} = (u, v, w)$ is the Cartesian mean velocity vector corresponding to the spatial coordinate vector (x, y, z); f is the Coriolis parameter; ρ is the density; P is the hydrostatic pressure; K_m is the vertical eddy viscosity; and F_u represents the horizontal momentum diffusion term. The horizontal diffusion term F_u is closed using the Smagorinsky eddy parameterization method, as described in more detail in [13]. The vertical eddy viscosity term K_m is modeled using

$$K_m = \ell q S_m \tag{2}$$

Here, l is the turbulent macro-scale; $q^2 = \frac{1}{2}(u'^2 + v'^2)$ is the TKE; and S_m is a stability function of Galperin et al. [38]. For more details about these variables and different constants, see [13].

2.2.2. Model setup

The unstructured model grid used in this study was initially developed by Rao et al. [39] as part of a tidal energy resource assessment study, which is further modified by Yang et al. [9] to include both the Bay of Fundy and the northern Gulf of Maine, shown in Fig. 1a. The model grid resolution varies from 20 m in the Western Passage to approximately 1 km near the Bay of Fundy and 2 km along the open boundary in the northern Gulf of Maine. The existing resolution exceeds the minimum model resolution of 50 m required by IEC TS 62600-201 for the Stage 2 design layout study. In both the previous studies, Rao et al. [39] and Yang et al. [9], the model bathymetry for the Western Passage was taken from the prior study by Xu and Xue [18]. In this work, we have updated the model bathymetry using the latest Eastern Canada 3 arc-second Bathymetric data [35] for the region. This data set provided a better representation of the shallow inter-tidal areas (Fig. 2) compared to the previous studies, even though the data resolution remained coarser (~90 m) than the unstructured model grid. The Passamaquoddy–Cobscook Bay archipelago is strongly dominated by tidal fluctuations; other forces such as river discharge, swell from the open ocean, and local wind-induced wave action are observed to have a relatively insignificant contribution to the overall flow patterns [9,39]. These negligible forces, along with the bit of source material for suspended sediment loads from the rocky shoreline and rock/gravel seabed [40], provide conditions for weak stratification and a well-mixed estuary [41]. Hence, during model setup, we neglected the sea surface wind, temperature, salinity, and baroclinicity effects in this study. Model simulations were carried out in a 3D, barotropic mode, where 15 uniform sigma layers were specified for the vertical direction. In addition, based on the velocity field data sets, which showed that the horizontal processes are an order of magnitude larger than the vertical, we selected the hydrostatic version of the model. The

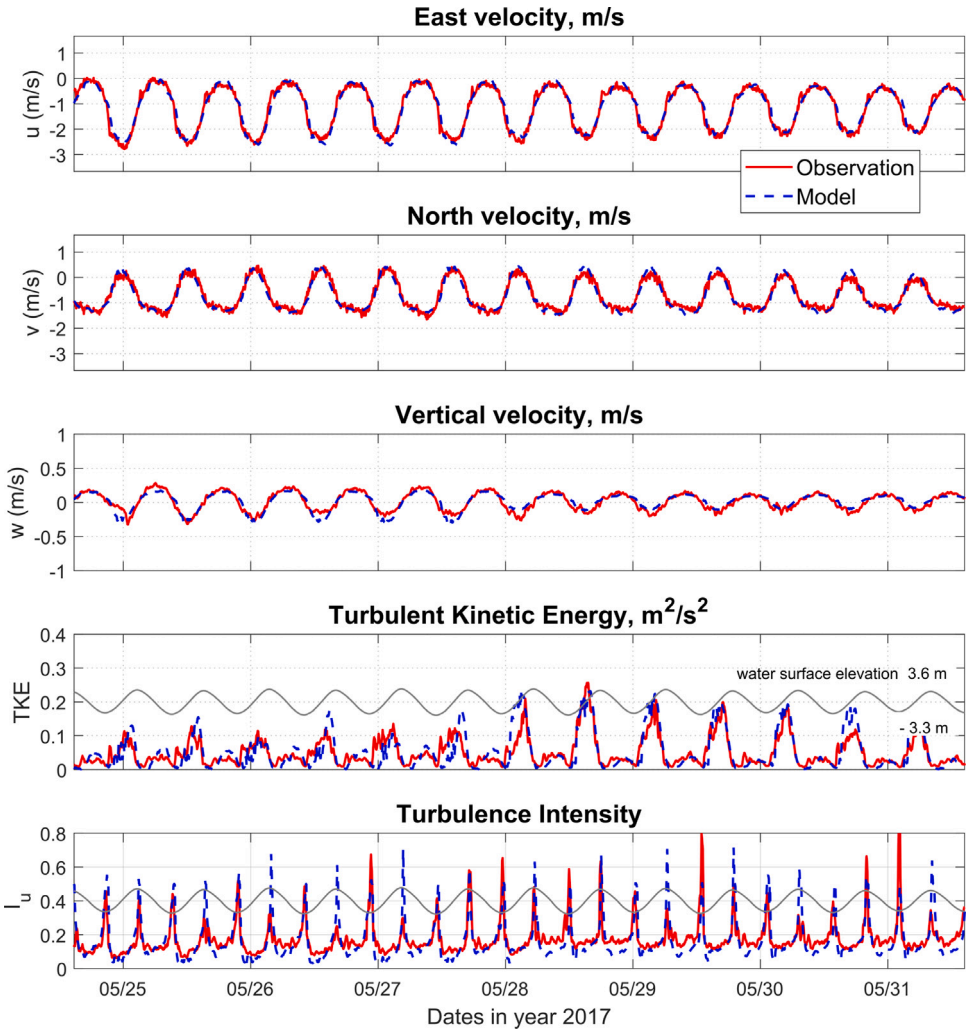

Fig. 3. Model performance comparison against the ADV dataset during a spring tide cycle at STTM location. Flow variables considered here are: eastward velocity, u (m/s); northward velocity, v (m/s); vertical velocity, w (m/s); turbulent kinetic energy, TKE (m^2/s^2); and turbulence intensity, I_u. The model results are shown in blue and in-situ in red. Water surface elevation (m) is shown using a gray line to better represent the flood and ebb cycles.

horizontal mixing coefficient in the Smagorinsky scheme, kept to 0.5, and a vertical mixing coefficient of 1.0×10^{-5} and a model minimum depth of 5 cm for wetting and drying are defined. Finally, to force the model from the lateral open boundary, we specified time-series of tidal surface elevation — generated using 13 tidal constituents (M2, S2, N2, K2, K1, O1, P1, Q1, M4, MS4, MN4, Mm, and Mf) from the TPXO 7.2 global ocean tide database [42].

2.2.3. Model validation

Initial validation of the Western Passage model were conducted using field data from three separate periods: July 2000, September 2001, and April–June 2017 [9]. Essential hydrodynamic variables such as water surface elevation, amplitude and phase lag of the tidal constituents, and current velocity were compared, and a good agreement between the model and field data was obtained in [9]. In the present study, we focused on the ADCP and ADV gauges located in the Western Passage (WP in Fig. 2) for further validation of the turbulence properties. We ran the model for a week (May 24, 2017–June 01, 2017) covering the STTM (ADV) deployment period and validated the modeled velocity, total TKE, and I_u.

The comparisons have been assessed in terms of the average bias index and model skill [43] (Eqs. (3)–(4)), where a model skill of 1.0 shows perfect agreement and a positive/negative bias represents model over/under-prediction, respectively:

$$Bias = \frac{\sum_{n=1}^{N}(M_n - O_n)}{\sum_{n=1}^{N} O_n} \tag{3}$$

$$Skill = 1 - \frac{\sum_{n=1}^{N}(M_n - O_n)^2}{\sum_{n=1}^{N}(|M_n - O| + |O_n - O|)^2} \tag{4}$$

where N is the total number of samples, M_n is the model result, O_n is the observed data, and O is the mean of the observed data.

Fig. 3 shows comparison between model and observation, where we can see good model agreement for all the 3D components. Especially, for the horizontal velocity components, the skill is much higher compared to the vertical component, ranging between 0.97 to 0.99 (Table 1). At the same time, we also found excellent agreement for the total TKE (Fig. 3), where it has an asymmetric distribution and is more prominent during the flood. The increase in TKE magnitude around May 28, 2017, observed in Fig. 3, came from the northward shift of the mooring. The instrument moved to a deeper portion of the channel, and we extracted the model output from the same location — at 10 mab. Subsequently, we estimated the model I_u using Eq. (5) [14] and compared it with the field data. This metric I_u is computed using the turbulent kinetic energy and mean flow velocity as

$$I = \frac{\sqrt{\overline{u'^2}}}{\sqrt{u^2 + v^2}} \approx \frac{\sqrt{q^2}}{\sqrt{u^2 + v^2}} \tag{5}$$

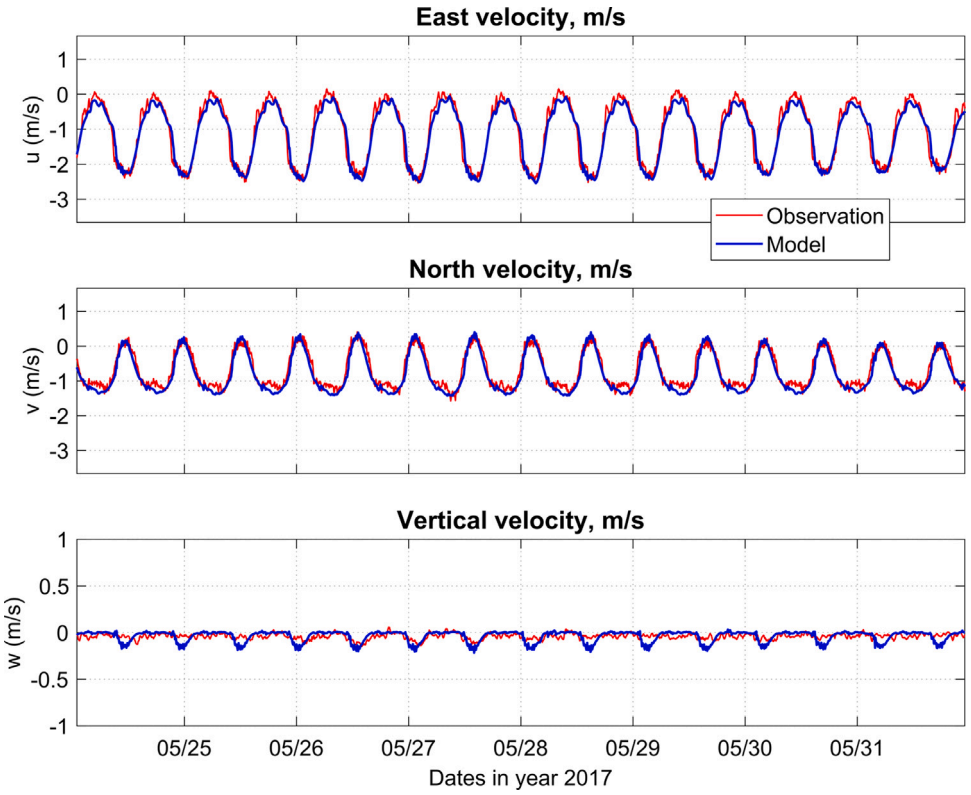

Fig. 4. Model performance comparison against the ADCP dataset at 10 mab near the STTM deployment — during the same spring tide cycle. Flow variables considered here are: eastward velocity, u (m/s); northward velocity, v (m/s); vertical velocity, w (m/s). The model results are shown in blue and in-situ in red.

Table 1
Comparison between model and in-situ velocity data in terms of model skill and averaged bias index at the STTM and ADCP locations in the Western Passage.

STTM location	Skill	Avg. bias index
u (m/s)	0.99	−0.037
v (m/s)	0.98	0.027
w (m/s)	0.95	−0.097
ADCP location		
u (m/s)	0.98	−0.110
v (m/s)	0.97	−0.004
w (m/s)	0.50	−0.031

Here, u' is the principal horizontal velocity fluctuation component; q^2 is the TKE, and u, v represent the velocity components described earlier.

The subplot at the bottom of Fig. 3 shows that for the major portion of the time-series, both field and model have a range of 10%–20%. The intensity increases significantly during the slack tide to almost 60% due to the much smaller mean flow velocity. In reality, during this short period of elevated unsteady load, the turbines will not operate when the cut-in speed is defined — typically above 0.8 m/s [4,5]. Finally, in addition to the STTM location, we also validated the model performance at the ADCP location in the Western Passage (Fig. 2). Fig. 4 shows the three velocity components at 10 mab, similar to the STTM location. While this gauge is closer to the shore than the STTM and shows a slightly reduced current, we still have observed a model skill close to ∼0.98 for u and v. The vertical velocity at this place is negligible compared to u and v due to the shallow conditions, reflecting a challenging environment for model predictions of vertical variation. The averaged bias index overall shows a slight model underprediction at both these locations.

3. Results and discussion

3.1. Identification of along-channel tidal energy hotspots

In the previous modeling study, Yang et al. [9] selected two hotspot locations to compare the vertical structure of the current magnitude and water depth distribution, one at the entrance of Western Passage and another at the end of Moose Island, based on the spatial distribution of the depth-averaged velocity. The resource assessment study has shown that both these locations have good potential for tidal energy extraction, where the tidal energy flux at the entrance of the Western Passage is much higher than the other, making it a favorable location for farm development. In this study, we picked six transect locations (XS-1 to XS-6) along the Western Passage (shown in Fig. 5) to analyze the variation in the vertical structure of the flow velocity and turbulence characteristics simultaneously. These locations are selected based on the time-averaged power density P_w, defined as

$$P_w = \frac{1}{1000} \cdot \frac{1}{N} \sum_{i=1}^{i=N} \frac{1}{2} \rho \mathbf{u}_i^3 \tag{6}$$

where, N is the total number of velocity output time steps; we used the depth-averaged velocity $\mathbf{u}$ for power density estimate and the time-averaging is done over the entire month.

We kept one transect (XS-1) right outside the entrance of Western Passage, between Moose Island and Indian Island, and a second transect (XS-2) at the entrance to see the effect of channel confluence on velocity shear and turbulence production during a flood tide. Then, we placed the last transect (XS-6) at the end of Moose Island to match the location used in [9]. Ultimately, these across-channel transects are assigned to help us rank suitable places for turbine farm development when all the essential flow characteristics such as flow velocity, TKE, and I_u are considered during different tidal conditions.

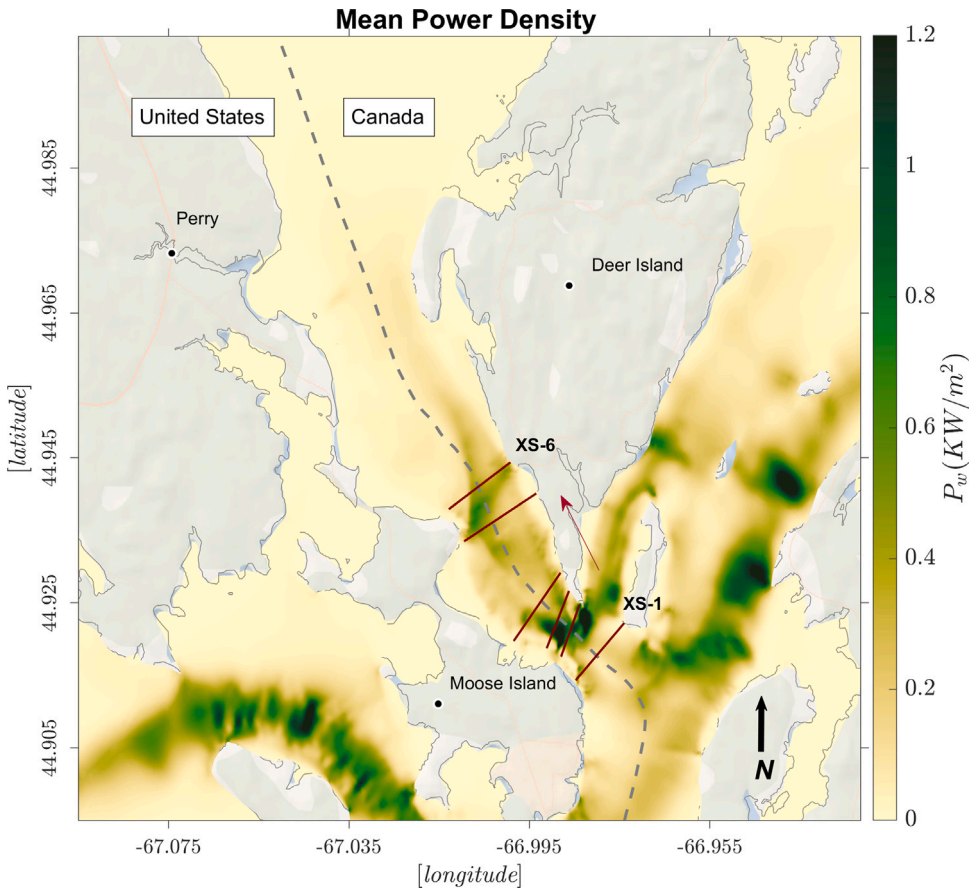

Fig. 5. Time-averaged power density, P_w (KW/m^2). Here, the depth-averaged velocity is used for the power density estimate, and the time-averaging is done over the entire month. Red solid lines represent six transect locations (XS-1 to XS-6) along the Western Passage, used for resource characterization and analysis of the flow structures.

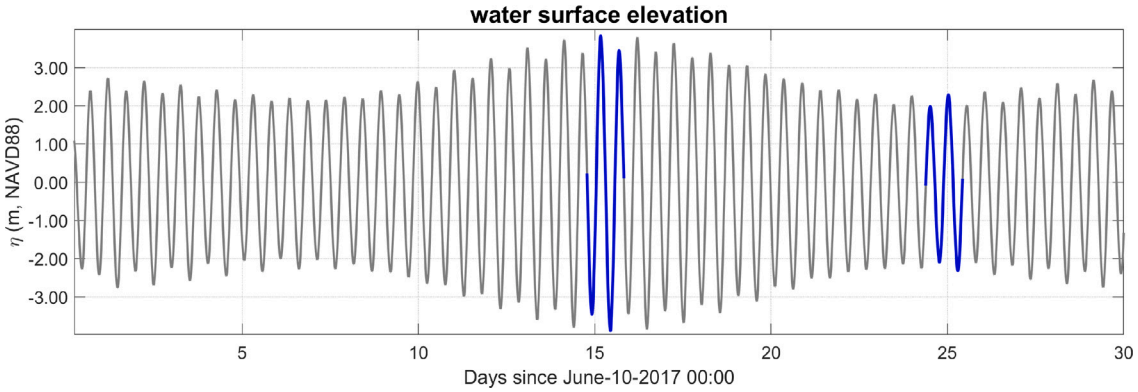

Fig. 6. Time series of month-long water surface elevation (in meters) at the entrance of the Western Passage. Two separate time windows representing spring and neap cycles are shown in blue, and are used later for time averaging of the flow variables.

3.2. Flow and turbulence characteristics

This section examines the vertical distribution of different flow quantities mentioned previously at the transect locations. As we have identified these places based on the time-averaged power density and have a qualitative idea of the theoretical power throughout the Western Passage (Fig. 5), for this analysis, we will specifically assess the following flow variables: tidal current speed, TKE, and I_u. Moreover, the Western Passage has a large spring-neap tidal variability where the tide range during the spring cycle is almost double that of the neap, as shown in Fig. 6. Thus, we evaluated the flow dynamics separately for the spring and neap conditions using daily averaged model results during both periods, as shown in blue in Fig. 6.

In the previous study, Yang et al. [9] found that there is 46 MW of theoretical power available at the entrance of the Western Passage. While this is a high-energy site for tidal farm development, the location has a complex flow condition due to the surrounding bathymetric features and channel confluence. We can clearly see the influence of the complex morphology on along- and across-channel flow behavior in Figs. 7 and 8. First, from the flow speed in Fig. 7, it is evident that the region has a higher flow condition during spring tide due to the higher tide range. Through the channel section at XS-1, between Moose Island and Indian Island, the power density is much smaller than the other channel — the Indian River, between Deer Island and Indian Island (Fig. 5). A similar flow characteristic is also seen in the cross-sectional speed distribution for XS-1 in Fig. 7.

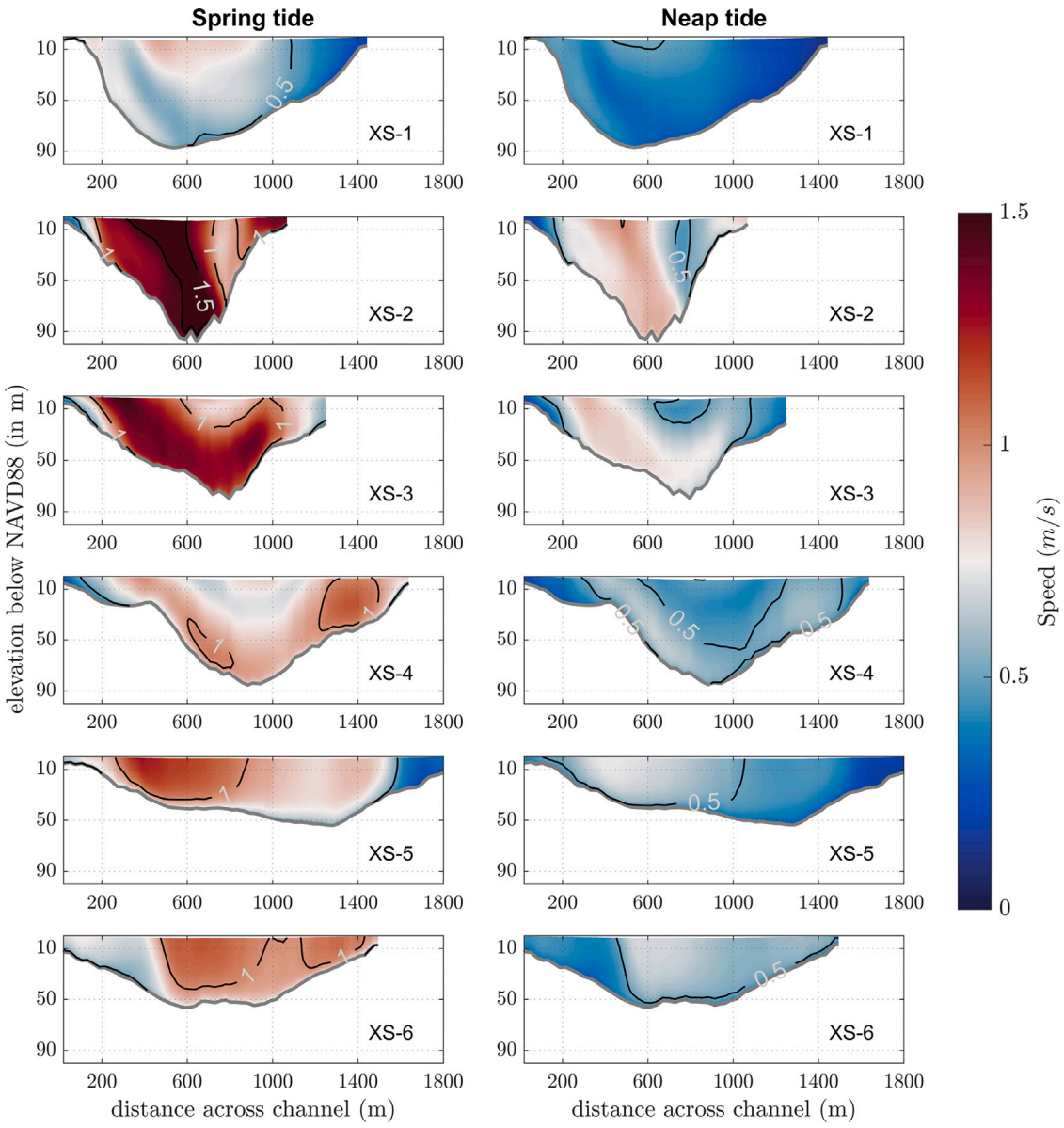

Fig. 7. Time-averaged flow speed (in m/s) for spring and neap cycles shown in Fig. 6 at different channel transect locations (identified in Fig. 5). All transects begin from the southwest side of the channel.

Figs. 8, 9, and 10 show the horizontal maps of depth-averaged peak current speed and TKE during spring flood and ebb cycles, and daily-averaged TKE and I_u at the transect locations, respectively. Fig. 8 shows that XS-1 at the stretch between Moose Island and Indian Island has an across-channel asymmetry for both speed and TKE. During flooding, the flow primarily enters toward the channel's left side (USA). A relatively higher tide-averaged TKE is observed, possibly generated from the headland and underwater sills located at the downstream end of this transect. During ebb, the flow comes out through the right side (Canada) of the channel and shows a higher TKE around mid-channel (Fig. 9). Interestingly, looking at I_u in Fig. 10, we can see that in the same location, even with the tide-averaged representation, I_u reaches 20%. The vertical variation of speed and TKE seems to play an essential role here, where it has higher turbulent fluctuations but a lower current speed from the mid to bottom portion of the transect.

At XS-2, right at the entrance of the Western Passage, the model results show a significant increase in the averaged flow velocity and TKE, reaching up to 1.5 m/s and 0.2 m^2/s^2, respectively, as shown in Figs. 7 and 9. The across-channel 2D variation of the flow speed and TKE shows a very complex pattern due to channel confluence and channel area contraction at the same time. Here, the channel becomes progressively narrower with a deeper thalweg, and the cross-section area decreases to 4.22×10^4 m^2 from 6.7×10^4 m^2 in XS-1. During the peak spring flood tide, the 3D fluid motion patterns in this section display the formation of a confluence hydrodynamic zone (Figs. 8c and 9), commonly seen at river networks where two incoming streams meet from different angles [23–26]. These studies have shown that when the two streams collide, a mixing interface develops between them, where large-scale turbulence coherent structures form within and close to that interface.

In the following Section 3.3, we discuss the formation and sensitivity of the turbulent structures to the momentum ratio (MR) and channel bathymetry of the colliding streams. Compared to the spring phase, during neap, the volume flux through the channels changes and immediately shows a decrease in the magnitude of speed and TKE at XS-2 (Figs. 7 and 9). At the same time, the averaged I_u across the channel (Fig. 10) is observed to be less sensitive to the spring or neap cycle, where it remains at 10% for the left side (USA) of the channel. However, we can also see that the magnitude has decreased compared to XS-1 during the spring.

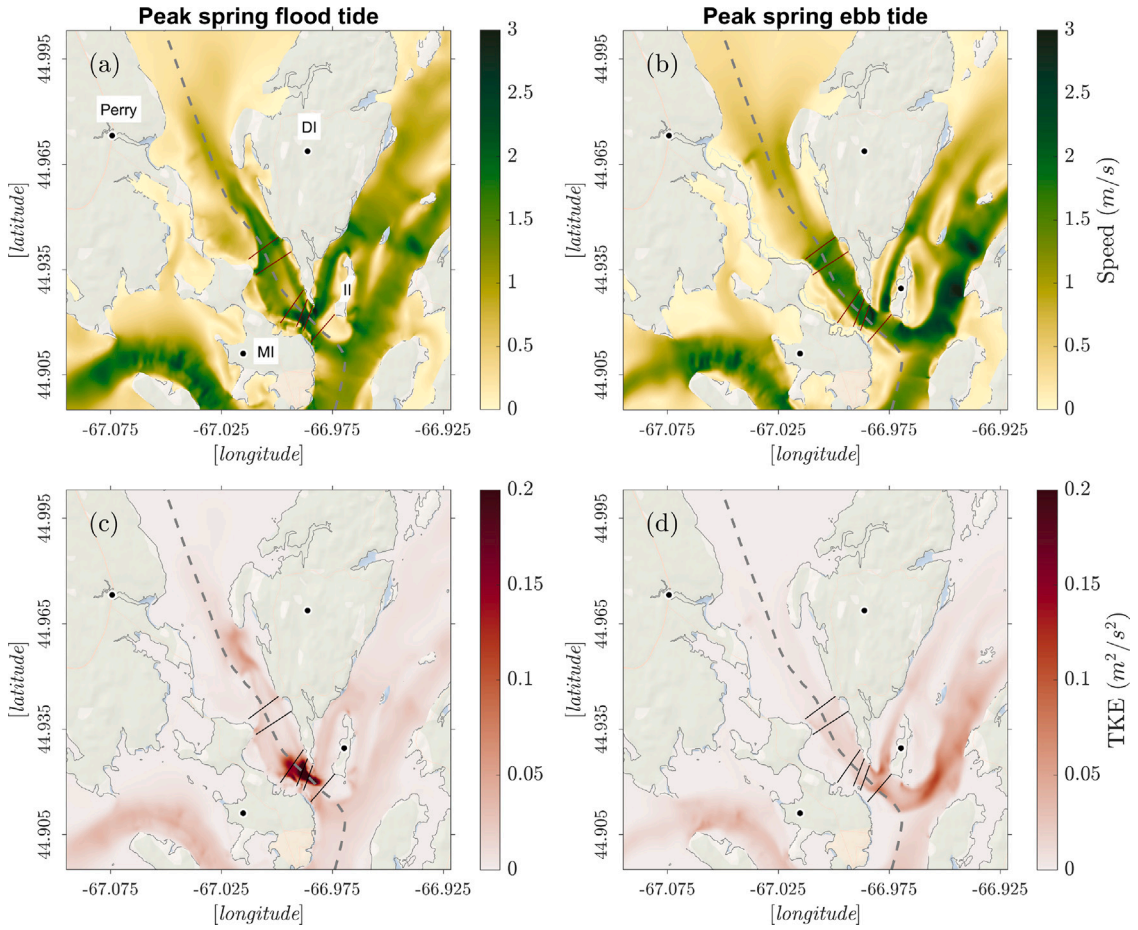

Fig. 8. (a,c) Spatial distribution of the depth-averaged speed (in m/s) and TKE (in m^2/s^2) - during a peak spring flood tide on June-25-2017; (b,d) similar analysis to (a,c) during the peak spring ebb tide.

At XS-3 and XS-4, the channel cross-section area gradually expands and shows a decrease in the peak speed along the channel, shown in Fig. 7. With this dramatic change in channel properties between XS-3 and XS-4, a bifurcation of flow occurs during the spring flood tide (Fig. 8a). Like XS-1, XS-4 shows a strong flow on the left side (USA) of the channel during the flood, which flips to the right side (Canada) during ebb. The TKE generated from channel confluence around XS-2 gets advected and dissipated as the flow travels upstream during the flood, where the jet effect diminishes near XS-4 (Figs. 8c and 9). Subsequently, while the pattern of along-channel flow change is similar during a neap condition, the magnitude decreases significantly, as shown in Figs. 7 and 9. Interestingly, the intensity comparison in Fig. 10 shows a different trend where an increase in the across-channel intensity can be seen at both XS-3 and XS-4. Both these sections display a more extensive spread of I_u, ranging from 5%–20%, where XS-4 has a higher unsteady loading close to the typical turbine hub height: ~10–15 m from the seabed [44,45]. Nonetheless, the increased I_u during the neap condition might not be an issue for the turbines; the flow velocity seems close to or below the cut-off speed (~0.8 m/s) generally used for activating the power extraction.

Finally, at XS-5 and XS-6, we can see a uniform distribution of speed where XS-5 has a more substantial flow in the channel's left side (USA). At the same time, the averaged TKE is almost non-existent compared to the other sections, shown in Figs. 8 and 9. The effect of this lower TKE and higher speed reflects on the I_u calculation in Fig. 10. At XS-5, we notice a small percentage (5%) close to the channel bottom, coming from the higher flow shear and the local turbulence production.

3.3. Sensitivity of turbulence characteristics to channel properties

In the previous section, we illustrated the complex time variation of speed, TKE, and I_u at several channel cross-sections in the Western Passage. In this section, we evaluate the role of the confluence hydrodynamic zone (Figs. 8c and 9) that forms at the entrance of the Western Passage near XS-2 in changing the downstream TKE and I_u distribution during flood tide. The confluence hydrodynamic zones form immediately within and downstream of stream junctions. Various studies [e.g.,22–26] have shown that the formation of complex 3D eddy motions in the mixing interface primarily depends on the velocity and momentum ratio of the two streams. This momentum ratio can vary based on crucial bathymetric features like channel and tributary cross-section areas, degree of concordance between the channel beds, underwater sills, and headlands at the entrance of the confluence zone. Constantinescu et al. [23] estimated this ratio using

$$M_r = \frac{\rho_1 Q_1 U_1}{\rho_2 Q_2 U_2} \tag{7}$$

where ρ_i, Q_i, and U_i are the density, volume flux, and cross-section averaged velocity, respectively, in the tributary [i = 1 (Indian River)] and main channel [i = 2]. To simultaneously compare the channel flow turbulence, we computed the Reynold's number as

$$Re = \frac{U D}{\nu} \tag{8}$$

where, D is the cross-section averaged depth and ν is the kinematic viscosity.

Fig. 11 shows a Google Earth image of the Western Passage confluence zone taken during a flood tide on August 27, 2017. The image

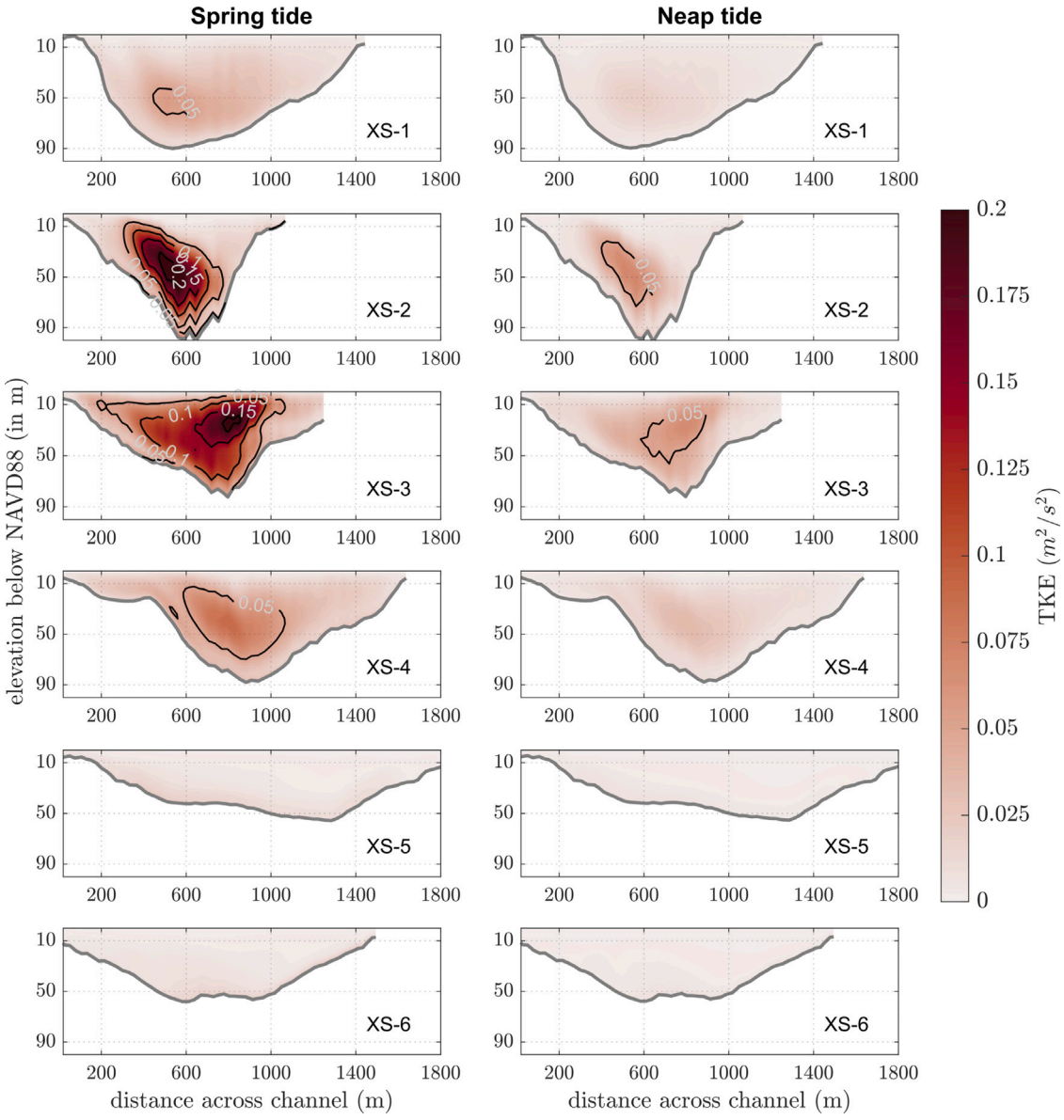

Fig. 9. Time-averaged turbulent kinetic energy, TKE (in m^2/s^2), for spring and neap cycles shown in Fig. 6 at different channel transect locations.

Table 2
Flow variables for Baseline case and Case-A during different flood tide conditions from the channels (Main channel and Indian River) before XS-2.

Baseline condition	Rising flood tide		Peak flood tide	
	Main channel	Indian River	Main channel	Indian River
Reynolds number, Re ($\times 10^8$)	1.93	3.50	2.57	4.36
Volume flux (m^3/s) ($\times 10^4$)	2.46	2.47	3.29	3.08
Cross-section avg velocity (m/s)	0.37	1.47	0.49	1.83
Momentum ratio, M_r	4.02		3.50	
Case-A	Rising flood tide		Peak flood tide	
	Main channel	Indian River	Main channel	Indian River
Reynolds number, Re ($\times 10^8$)	2.80	2.05	3.57	2.92
Volume flux (m^3/s) ($\times 10^4$)	3.60	1.49	4.57	2.06
Cross-section avg velocity (m/s)	0.54	1.34	0.68	1.88
Momentum ratio, M_r	1.03		1.26	

displays the horizontal distribution of the surface roughness during a particular flooding period and the formation of the confluence hydrodynamic zone and turbulent eddies in its mixing interface around XS-2. We can also see that the flow through the Indian River tributary behaves like a jet on the left side (Deer Island) and forms higher turbulent motion right before converging on to the main river. Interestingly,

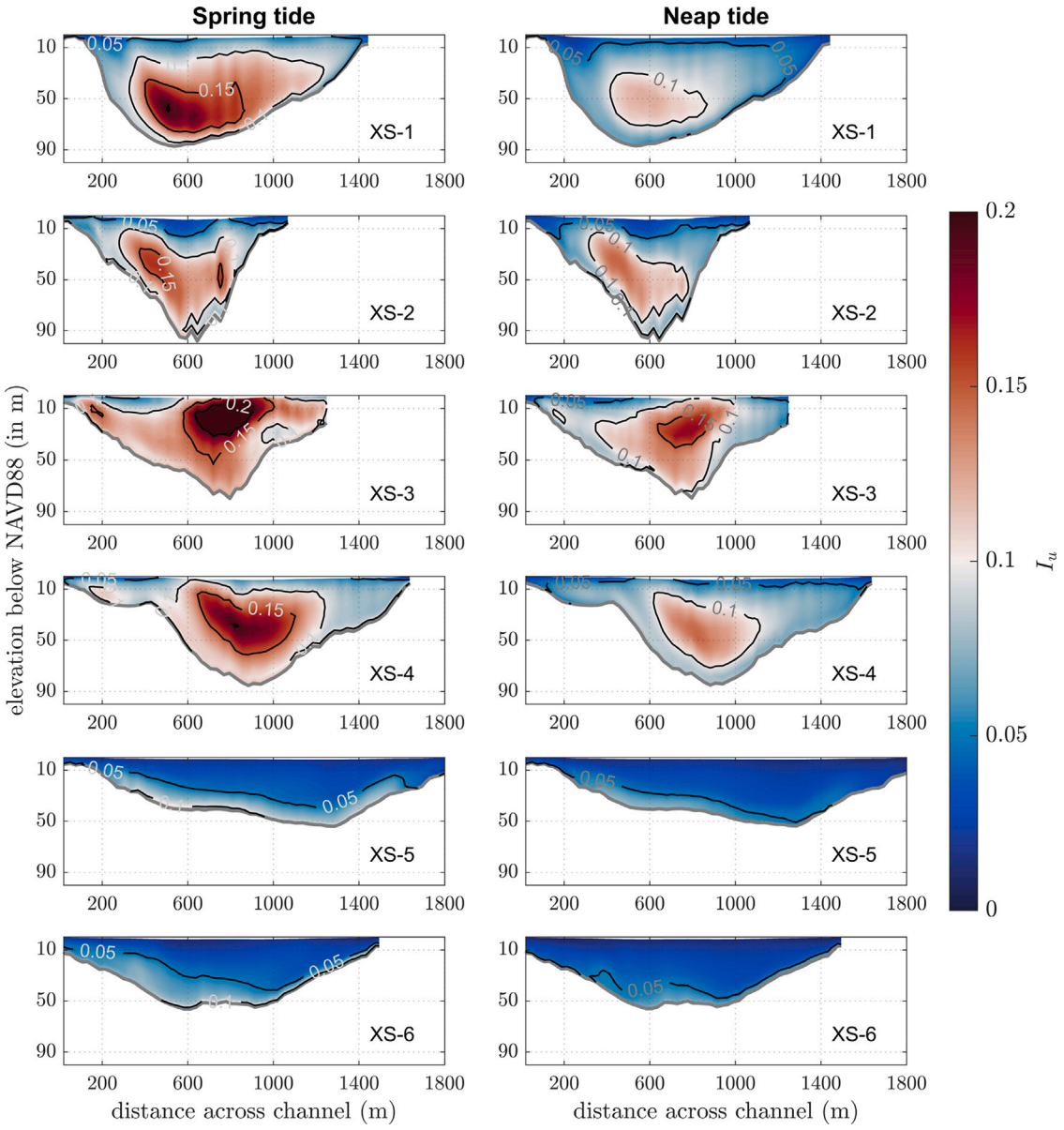

Fig. 10. Time-averaged turbulence intensity, I_u, for spring and neap cycles shown in Fig. 6 at different channel transect locations.

looking at the bathymetry in Fig. 12a (baseline), we can see that there is an underwater sill that extends ~300 m from the Deer Island headland, where the average depth is close to 12 m. This complex feature can contribute to the convective acceleration of the flow and the subsequent turbulent fluctuations in the confluence zone. In this study, we have developed two simple scenarios to investigate the effect of M_r during a flood tide and sharp bathymetry change from the underwater sill on turbulent flow structure at the confluence hydrodynamic zone, XS-2. In case-A, we have reduced the maximum depth (~35 to 45 m) in the Indian River (considered as a tributary) between Deer Island and Indian Island to 20 m [Fig. 12a (case-A)]. This change to the tributary cross-section area would reduce the volume flux Q through Indian River, alter M_r, and ultimately affect the instabilities in the mixing interface. For the other scenario, case-B, we removed the underwater sill south of Deer Island by providing a depth similar to the main channel, shown in Fig. 12a (case-B), to evaluate its role in producing turbulent fluctuations near XS-2. These scenarios are compared against the baseline model simulation, which was validated using field data and is discussed in the previous section.

3.3.1. Baseline case

As shown earlier, the TKE at XS-2 is prominent during the spring flood tide, and we picked two instantaneous times during flood shown in Fig. 12b for this analysis. Figs. 13 and 14 show a comparison of depth-integrated speed and TKE between different scenarios, during rising and peak flood tide, respectively. The vertical shear of the horizontal velocity and vertical eddy viscosity that control the local turbulence production are shown in Figs. 15 and 16. In Fig. 13, for the baseline case, we can see that the tidal wave propagates faster through the Indian River than the main channel at the beginning of the flood. Also, there is an increase in flow velocity over the underwater sill, south of Deer Island, due to the rapid bathymetry change (Fig. 13a, top). Right before the confluence zone, Re at the main channel and the Indian River tributary is observed to be 1.93×10^8 and 3.5×10^8, respectively (Table 2). At the same time, we estimated the tributary-channel momentum ratio (M_r) to be 4.02. Fig. 13b (top) shows the initiation of higher TKE at the northern end of XS-2 while the speed decreases. After passing through the narrow passage XS-2, flow shows a diversion toward the left side of the main channel, and clockwise and counter-clockwise eddies form on both sides, representing the flow

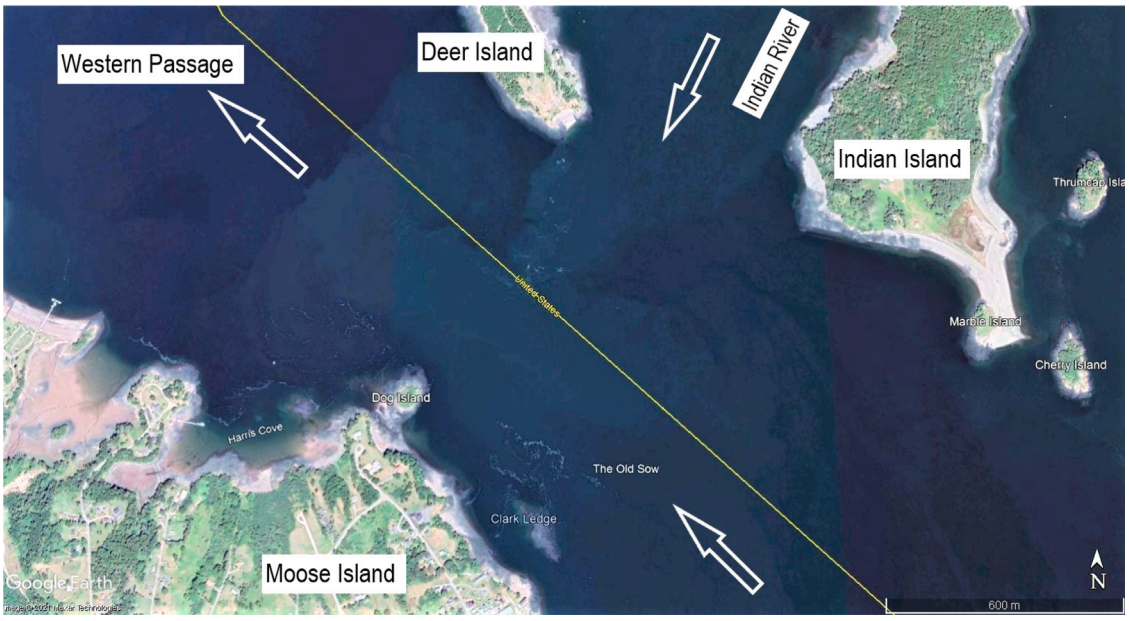

Fig. 11. The horizontal distribution of the surface roughness during a particular flooding period on August-27-2017, taken from the Google Earth database, shows the formation of a confluence hydrodynamic zone and turbulent eddies at the entrance of the Western Passage. The white arrows represent the flow direction.

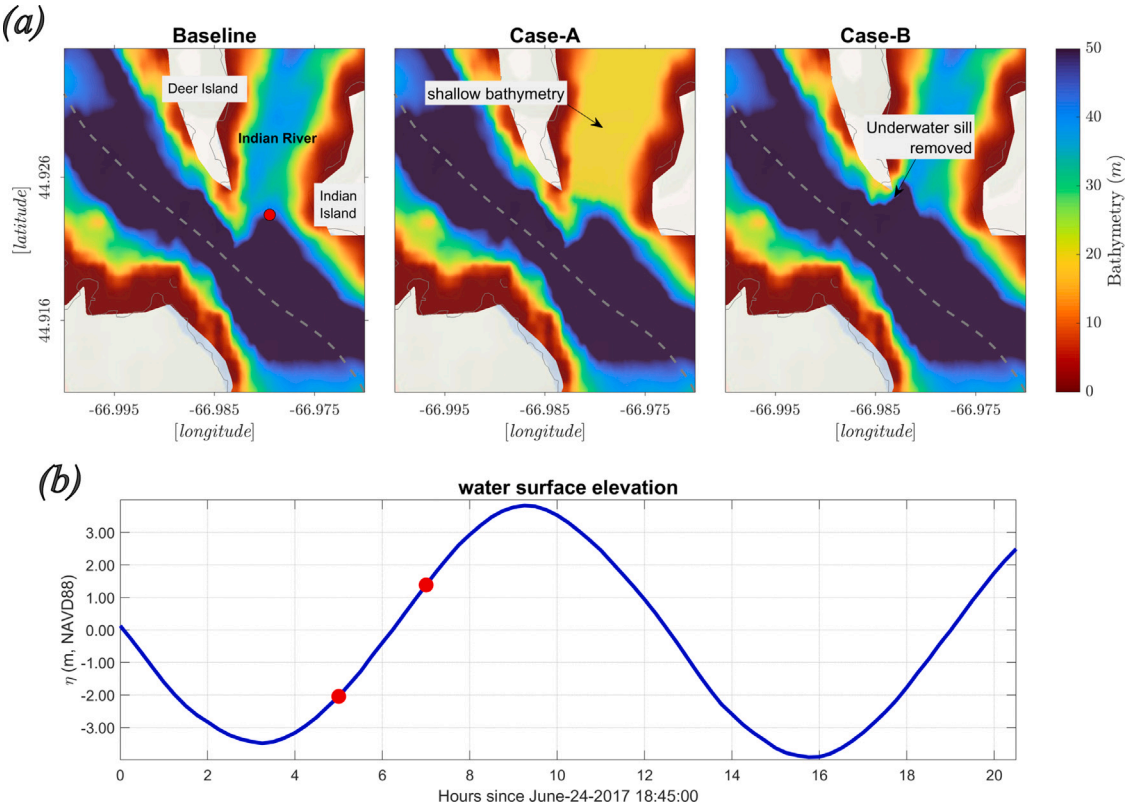

Fig. 12. Bathymetry scenarios to investigate the effect of tributary-channel momentum ratio and underwater sill on turbulent flow structure at the confluence hydrodynamic zone, where (a) left (Baseline): the existing model bathymetry (in meters, from NAVD88); middle (Case-A): the Indian River tributary maximum bathymetry reduced to 20 m; right (Case-B): removal of the underwater sill near the Deer Island headland, and (b) instantaneous time windows used for comparing turbulence properties at the confluence zone (XS-2) shown later in Figs. 13–16.

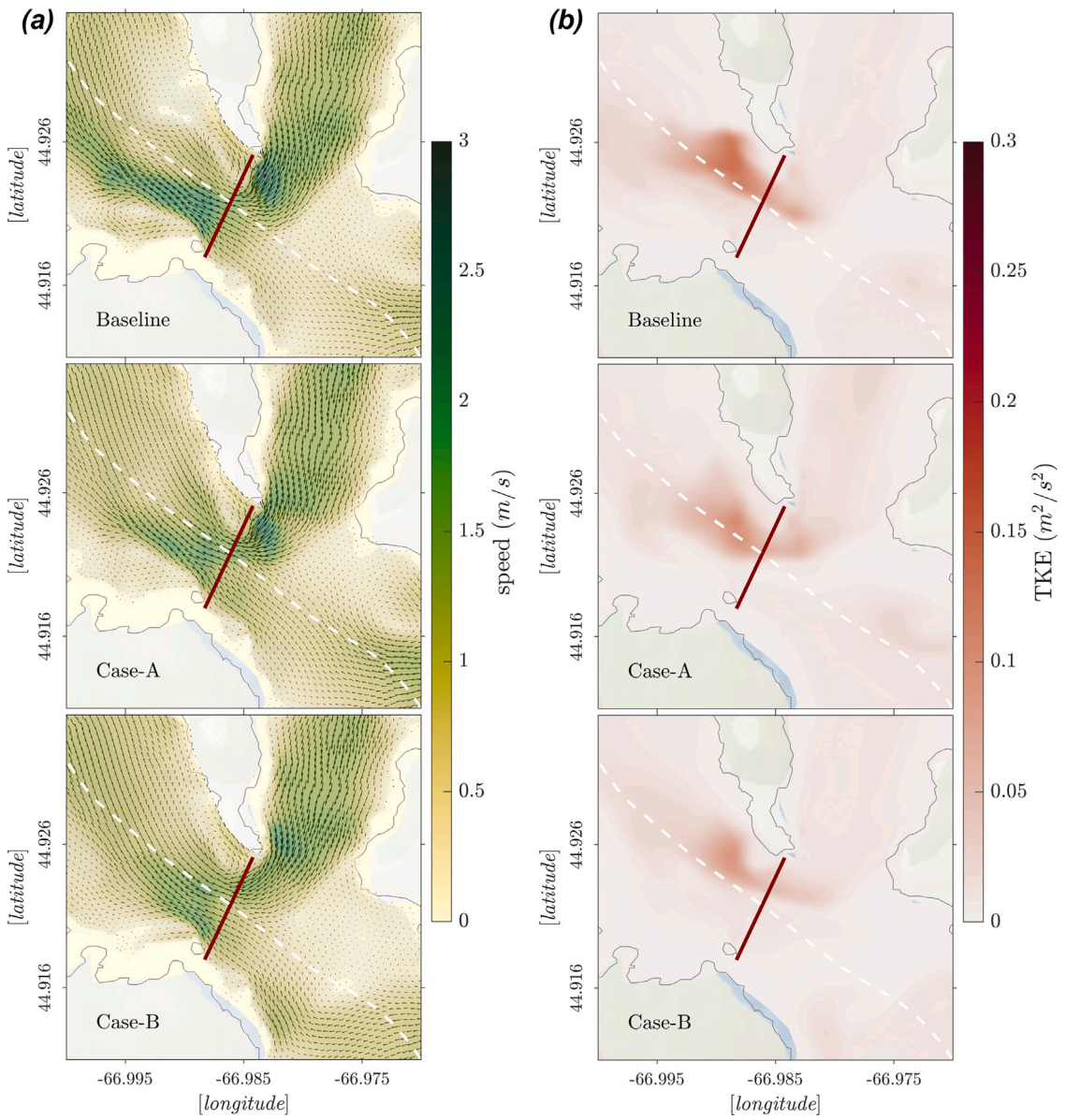

Fig. 13. (a) Depth-integrated speed (in m/s) for different scenarios during the rising flood tide (first red circle in Fig. 12b) in the channel confluence zone and around XS-2; (b) depth-integrated TKE (in m^2/s^2) for different scenarios during the rising flood tide. The red solid line represents the channel transect XS-2.

separation. During peak flood, shown in Figs. 12b and 14b (top), Re at both channel and tributary becomes 2.6×10^8 and 4.4×10^8 and M_r is equal to 3.5 (Table 2), producing a much greater level of turbulence at the confluence zone. Consequently, a flow bifurcation is observed when the channel expands behind XS-2, producing two eddies on the sides.

The shear production term of the TKE, P_s, is related to the vertical shear of horizontal velocity (U_z) and the vertical eddy viscosity (K_m) as

$$P_s = -\overline{u'w'}\frac{\partial u}{\partial z} - \overline{v'w'}\frac{\partial v}{\partial z} = K_m U_z, \quad U_z = \left(\frac{\partial u}{\partial z}\right)^2 + \left(\frac{\partial v}{\partial z}\right)^2 \tag{9}$$

To assess the vertical variability of local turbulence production at XS-2, we have separately explained U_z and K_m for the flood events, shown in Figs. 15 and 16. With the baseline case, during both rising and peak tide, there is a strong vertical shear observed on the mid to left portion of the channel, where U_z reaches 0.08 s^{-2} during peak tide. At the same time, we notice a very large K_m - greater than 1.5 m^2/s - potentially from the merging of the advected turbulent eddies from the confluence zone. Constantinescu et al. [23,24] have used detached eddy simulation (DES) with the Spalart–Allmaras (SA) RANS model to assess the formation of 2D and 3D eddies in a river confluence zone. They have shown the generation of large-scale quasi 2D eddies in the mixing interface for both 'wake mode' ($M_r \sim 1$) and 'Kelvin–Helmholtz (KH) mode' ($M_r \gg 1$) instabilities that break down while being advected in the downstream and forms a region with highly 3D energetic eddies (See Figs. 14 and 15 in [23]). In this study, we are not resolving such a range of scales and are only describing turbulence characteristics by solving macroscale [27,28] where the energy is concentrated (i.e., peak in the energy spectrum). From Figs. 15 and 16, we can see that there is still local turbulence production at XS-2, downstream of the confluence zone, and very prominent during the peak flood tide.

3.3.2. Case-A: Changes to tributary-channel momentum ratio

In this scenario, during rising tide, while the depth-integrated velocity magnitude and direction through the Indian River tributary increased slightly compared to the baseline (Figs. 13, case-A), Re at Indian River decreased to 2.05×10^8 and M_r decreased to 1.03. We can see a change in depth-integrated TKE and the flow field behind XS-2, where both became weaker. From the across-channel U_z and K_m

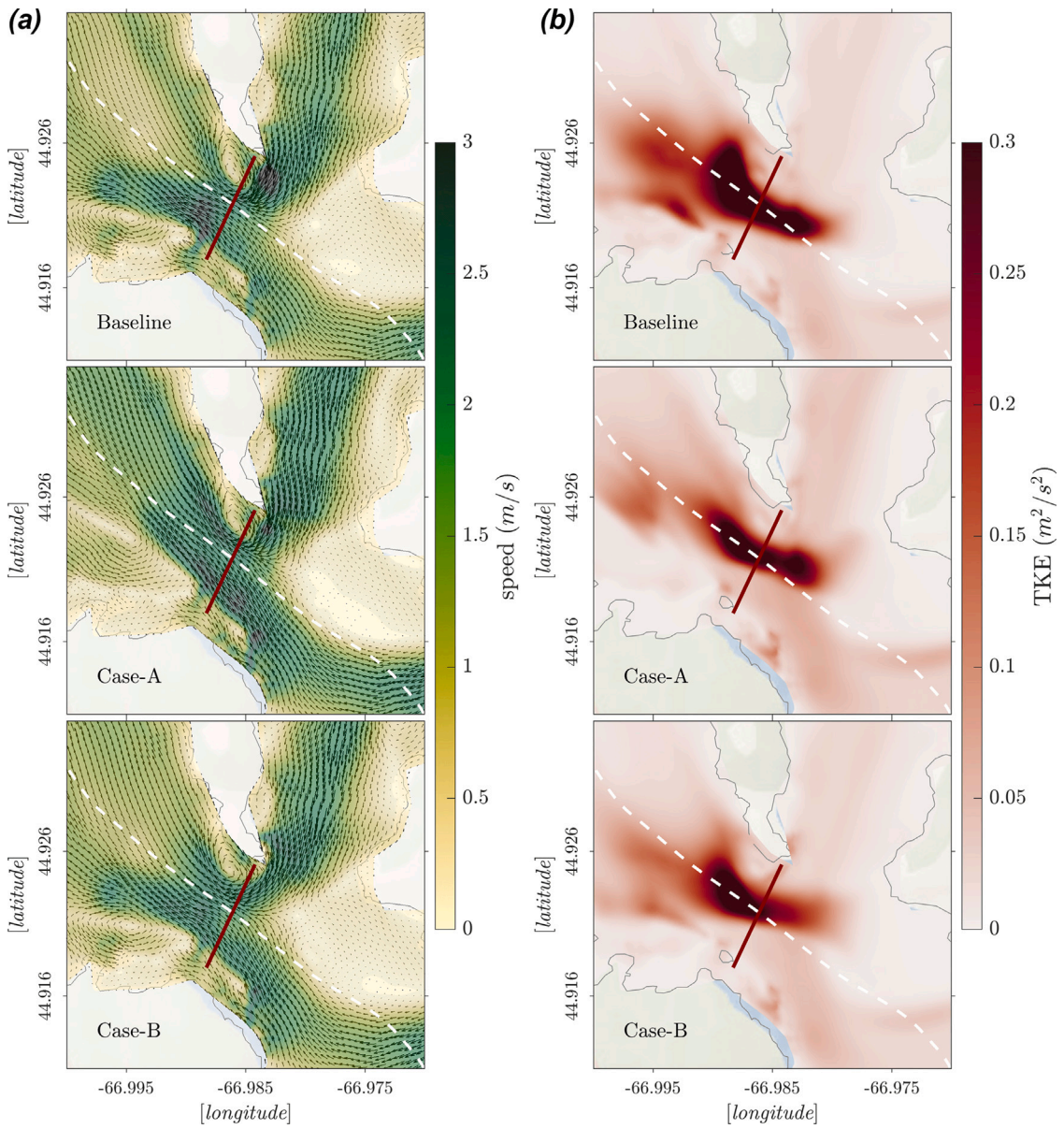

Fig. 14. (a) Depth-integrated speed (in m/s) for different scenarios during the peak flood tide (second red circle in Fig. 12b) in the channel confluence zone and around XS-2; (b) depth-integrated TKE (in m^2/s^2) for different scenarios during the peak flood tide. The red solid line represents the channel transect XS-2.

comparison shown in Figs. 15 and 16 (case-A), it is evident that with a reduced volume flux from the tributary, U_z and K_m both decreased at XS-2, resulting in less production of turbulence. At the same time, this scenario also represents a higher bed elevation discordance between the main channel and the tributary that changed the velocity shear in the confluence zone. We can see its effect in the U_z distribution shown in Fig. 16 (case-A): the shear production has increased on the upper portion of XS-2 that matches the upstream modified Indian River bed elevation. Now, the reduction of the turbulent energy in the far-field of XS-2, shown in Fig. 14b, is an amalgamation of many factors. Especially, the reduced M_r (1.03) leading to a more unidirectional flow through the Western Passage (Fig. 14a) and the lessened depth-varying shear production from channel discordance, both contributed to shrink the turbulent plume.

3.3.3. Case-B: Underwater sill and tributary flow convergence

While the previous scenario (Case-A) illustrated the reduction in turbulent flow in the far-field of the confluence hydrodynamic zone, Case-B showed how an underwater sill, located on the tributary mouth, has increased the turbulence production (Fig. 14b, case-B). We noticed earlier in Figs. 13a and 14a that for the baseline case, during both rising and peak flood tide, the shoaling of the flow over the underwater sill generates a convective acceleration. If we remove this underwater sill as shown in Figs. 12a, the velocity magnitude immediately decreases around the headland before reaching the confluence zone. Fig. 14a shows that the minimized tributary flow acceleration can significantly reduce TKE production at the mixing interface (before XS-2), even though M_r and Re are similar to the baseline. Also, during both rising and peak flood tide, more flow takes a right turn close to the headland in the absence of the sill, decreasing the mid-channel shear production (Figs. 15 and 16). However, at XS-2, we can still see an across-channel distribution of eddy viscosity and TKE convergence similar to case-A (~1.5 m^2/s) from the channel width contraction.

4. Implications for tidal farm site selection

Designing TECs and identifying suitable deployment locations in energetic tidal channels is a complex problem that requires collaboration between device designers and project developers. While the

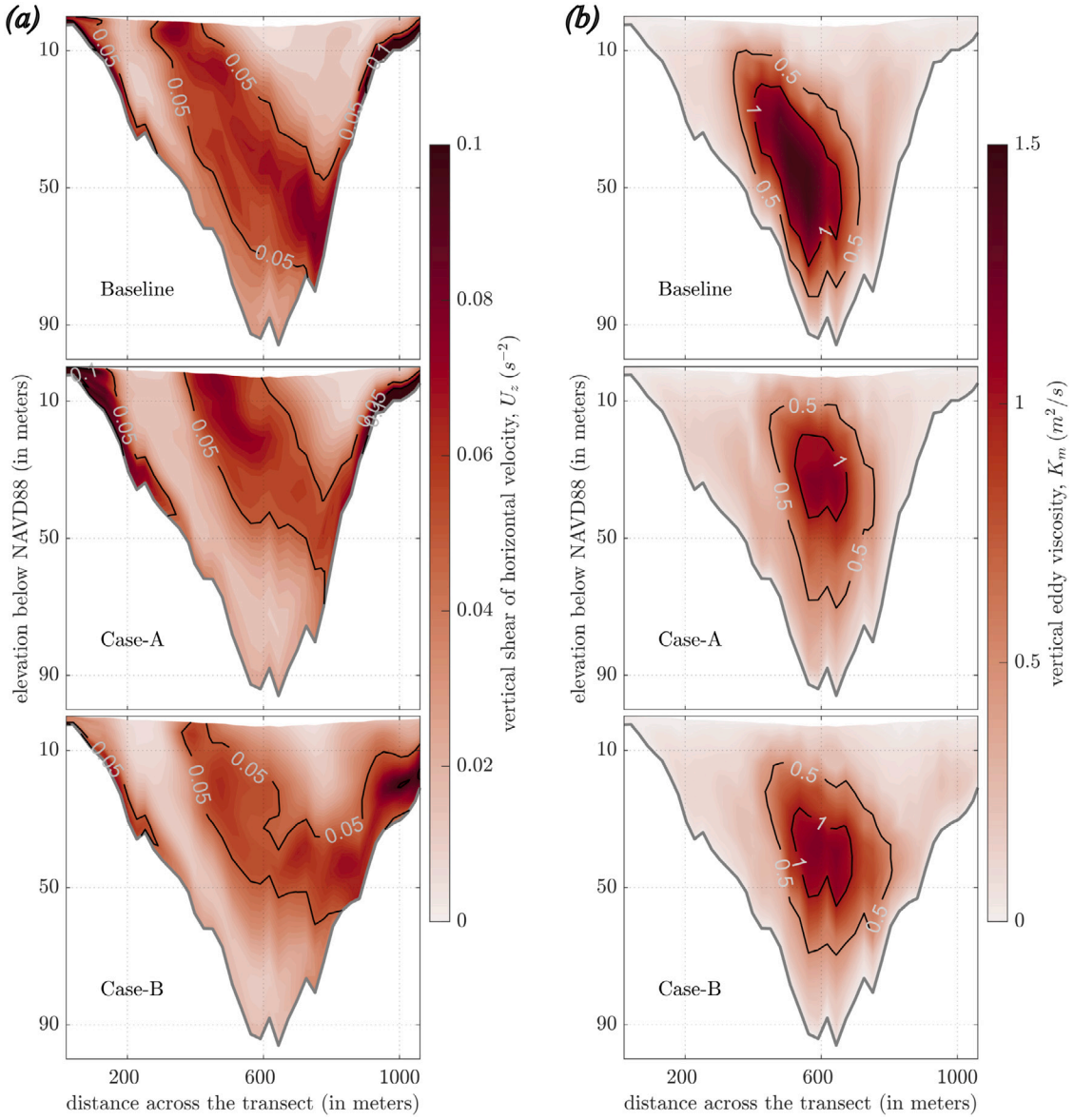

Fig. 15. (a) Vertical shear of horizontal velocity, U_z (s^{-2}), and (b) the vertical eddy viscosity, K_m (m^2/s), at XS-2 for different scenarios during the rising flood tide. Transect begins from the left side of the channel (Moose Island).

former seeks to optimize device design, the latter is concerned with finding economically viable sites and optimizing arrays of devices [21]. The tidal stream energy sites are highly turbulent and large- and small-scale turbulent motions can significantly impact power extraction efficiency and device fatigue [7,46,47]. While undisturbed channel tidal power density and Annual Energy Production (AEP) are commonly used to assess the regional-scale tidal energy resource [e.g.,3,4,8], these metrics do not account for the effects that turbulence can have on device and array performance. In particular, turbulence is generally understood to both reduce device power performance (especially near or above the device's rated speed), and also to reduce structural performance because of the increased fatigue cycles caused by unsteady loading [48–50]. Therefore, siting projects at locations with lower turbulence intensity will be advantageous.

Although our study did not resolve the inertial sub-range of turbulence (device-scale turbulent eddies), we proposed using macro-scale turbulent properties such as TKE and I_u to provide additional information for ranking potential sites when using regional-scale modeling frameworks for resource assessment. Because this macro-scale turbulent energy must cascade through the inertial subrange, and because this cascade has been shown to happen over relatively short temporal and spatial scales (compared with the scale of most tidal energy channels), it follows that more large-scale turbulence at a site also means more small-scale turbulence [51]. Our high-resolution 3D HPE model, employing the MY2.5 turbulence scheme, demonstrated excellent agreement with observed TKE and I_u in the Western Passage, suggesting that regional-scale models can reliably estimate peak energy-containing eddies. Previous studies by Thyng et al. [14] and Guerra et al. [15] also utilized similar 3D HPE modeling frameworks for resource assessment in energetic tidal streams, where estimates of TKE and I_u using macro-scale turbulence were found useful for TEC siting arrangements. However, these studies only examined I_u variation at the measurement location and did not explore the across and along channel changes in I_u, which provides further insight into the spatial distribution of turbulence intensity.

In this work, we simultaneously estimated TKE and I_u from different channel transects (XS-1 to XS-6) in the Western Passage to compare them with the tidal current speed to add more insight into the site selection for TEC siting. Among all our channel transects, we have observed

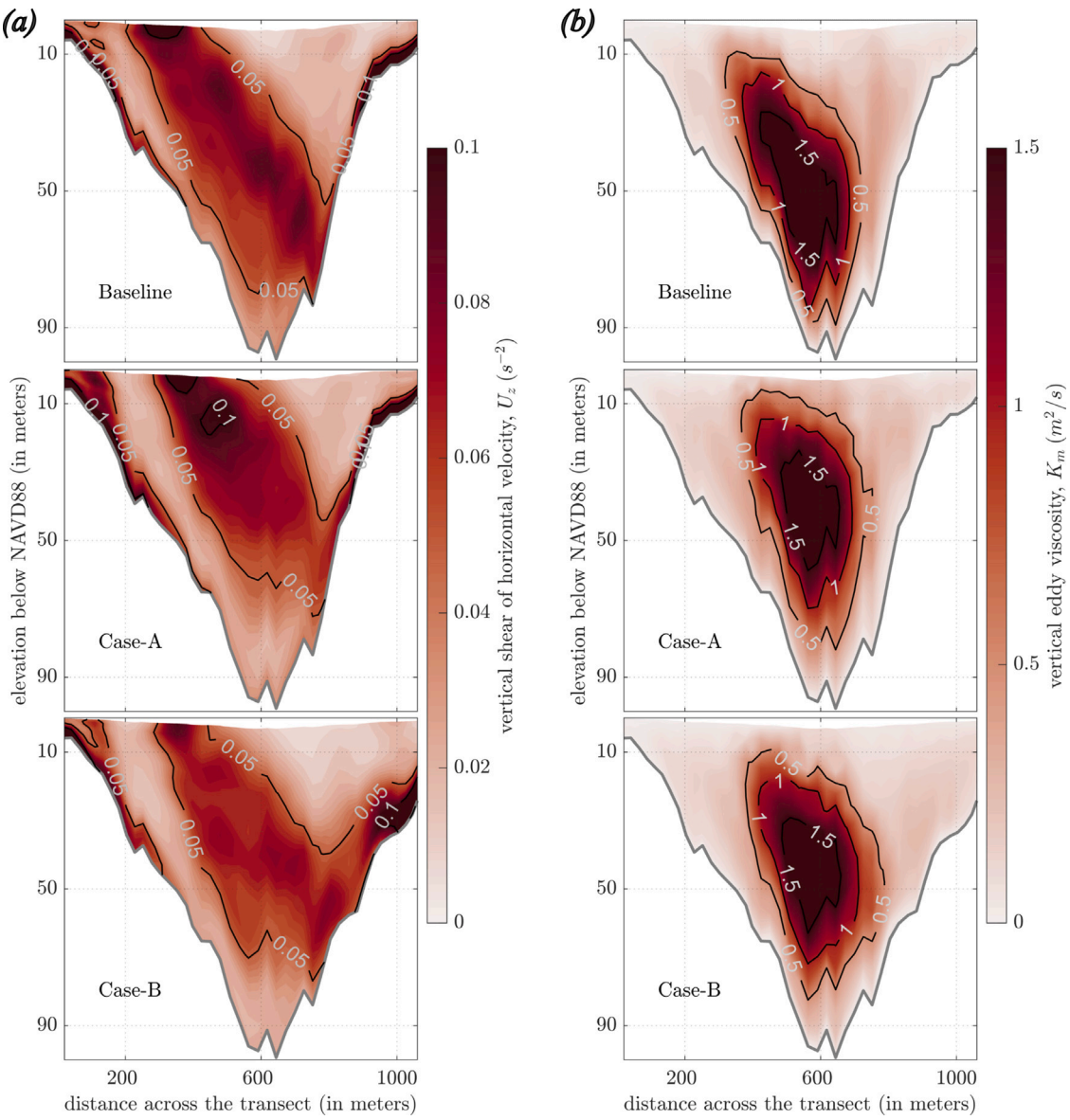

Fig. 16. (a) Vertical shear of horizontal velocity, U_z (s^{-2}), and (b) the vertical eddy viscosity, K_m (m^2/s), at XS-2 for different scenarios during the peak flood tide.

that XS-2, XS-3, and XS-5 show the higher mean power density and across-channel flow speed available to the US side. However, at XS-2 and XS-3, the time-averaged TKE and I_u are an order of magnitude higher than XS-5 due to the formation of the confluence hydrodynamic zone and an underwater sill at the entrance to the Western Passage. XS-5 appears to be less turbulent because it is not a confluence zone, is farther from the headland, and the seafloor is relatively smooth.

This suggests that XS-5 may be a more suitable site for deploying TEC devices – especially early prototypes – despite having half the kinetic energy flux of XS-2 (more details given in [9]). Wherever devices are deployed, it is critically important to measure both the turbulent inflow to the device and the device loads so that we can begin to understand the impact of turbulence on device performance (both power and structural). As we build up a collection of such datasets they will become increasingly valuable for validating not only device simulation tools, but also potentially to calibrate models like the ones used here to inform array planning. For example, we might learn that when high-resolution 3D HPE models estimate $I_u > 0.2$, the site is uneconomical but when $I_u < 0.1$ the site is economically promising.

This study also explored the impact of significant bathymetric features, such as the confluence zone and underwater sill, on local turbulence production in the Western Passage. However, higher-resolution LES models are necessary to gain a more comprehensive understanding of the intricate seabed morphology's effect on turbulence generation. Such models can offer critical metrics, including Reynolds shear stress components, turbulent dissipation rate, and vertical integral length-scale, essential for TEC design [52,53]. Nonetheless, despite their potential advantages, LES models are still not commonly employed in tidal resource assessment studies due to the extensive spatial (e.g., estuary) and temporal (e.g., spring/neap cycles) scales required and the associated computational expenses [54]. Recently, Bourgoin [55] and Bourgoin et al. [52] implemented a coupled unstructured grid LES-RANS model for a tidal turbulence study at Alderney Race. While these works have simulated the turbulence structures at a lower computational cost than standard Navier–Stokes formulations, the model accuracy is observed to be extremely sensitive to the unstructured grid aspect ratio and the adequate representation of near-wall physics and boundary conditions [56,57]. Using unstructured grid LES-RANS models in regional-scale tidal turbulence modeling continues to be a matter of ongoing research; it needs more studies focusing on model

calibration and validation to ensure accurate and reliable results. Our bathymetry scenario analysis showed that, even with the various limitations, 3D RANS models with Boussinesq and hydrostatic approximations could help understand the macro-scale turbulence production and aid in ranking the TEC siting locations. Complex locations consisting of confluence hydrodynamic zone and underwater sill should be avoided for TEC deployment due to the potential negative impact on the power extraction efficiency and device fatigue. Ultimately, the turbulence parameters (TKE and I_u) estimated at different channel transects and a detailed analysis of the flow characteristics have changed the site-ranking results in the Western Passage and introduced a new perspective to the overall characterization of tidal energy sites.

5. Conclusions

The numerical model results presented in this study have provided an opportunity to apply several critical macro-scale turbulence parameters in tidal channel resource characterization along with the traditional hydrodynamic variables. For this case study, we chose a top-ranked in-stream tidal energy site in the US – Western Passage, ME – that also consists of the Western Hemisphere's largest tidal whirlpool, Old Sow. We selected FVCOM, an unstructured grid, 3D ocean model for the modeling analysis of the complex tidally-varying channel flow structures. The IEC TS 62600-201 guideline is followed in the field data collection campaign, conducted in the same area, which we later put together for our model calibration and validation of essential flow variables. The model comparison against the observation showed excellent agreement throughout the data collection period. This comparison highlighted the performance of FVCOM (3D HPE) and the turbulence length-scale model MY2.5 in providing a reasonable assessment of the macro-scale kinetic energy, TKE and turbulence intensity, I_u at different channel depths. Then, we used the model results to show that using these channel turbulence properties can deliver necessary information during the evaluation of suitable cross-sections for TEC deployment. Mainly, the estimate of along- and across-channel vertical variation of the TKE and I_u added a new perspective for the potential TEC site ranking approach and can be helpful for future regional-scale site characterization studies. We also developed two hypothetical scenarios to illustrate the channel configuration's role in enhancing the sheared flow and turbulent eddies in potential TEC siting locations. These scenarios have shown that the turbulence production could be highly sensitive to channel confluence zone attributes such as the momentum ratio between tributary and main channel and underwater sills near headlands.

Additionally, the fact that our current 3D HPE model setup agrees with high-quality turbulence measurements suggests that it can be helpful in understanding which specific locations within a tidal channel are most promising for tidal energy device siting, and also suggests that similar models can be used to compare turbulence between different channels. This is important because, at present, the tidal energy community relies exclusively on turbulence measurements to identify whether a site is more or less turbulent than another. If, on the other hand, we are able to begin to trust regional-scale models to tell us what turbulence levels to expect at a site, it will dramatically improve our ability to identify and select the most promising sites. For the time being, we believe it is best to continue cautiously in terms of trusting the actual turbulence levels these models predict, and to continue to make measurements to validate the models before large investments are made (e.g., in deploying tidal arrays). But, as we continue to build confidence in 3D HPE models through these measurements, the models themselves will become increasingly valuable for siting projects and designing arrays. Coupled LES-RANS frameworks can help to further refine our understanding of turbulence in tidal channels. The LES models will provide the higher-accuracy statistics necessary for TEC device design purposes, and the 3D HPE models can help to guide the application of LES efforts (i.e., where LES models should be used). That being said, our implemented 3D HPE modeling framework is not fully complete in terms of representing all processes, and it will require a separate study in the future to investigate the other contributions from wind waves, stratification, and non-hydrostatic pressure in the overall flow structure. Ultimately, even with the current limitations, this work has provided valuable information about the flow and turbulence conditions in an energetic system and illustrated how a high-resolution regional-scale modeling approach could aid in TEC site ranking and resource characterization.

CRediT authorship contribution statement

Mithun Deb: Conceptualization, Methodology, Software, Visualization, Validation, Investigation, Writing – original draft. **Zhaoqing Yang:** Conceptualization, Methodology, Supervision, Project administration, Funding acquisition, Writing – review & editing. **Taiping Wang:** Validation, Software. **Levi Kilcher:** Data curation, Funding acquisition, Writing – review & editing.

Declaration of competing interest

The authors declare that they have no known competing financial interests or personal relationships that could have appeared to influence the work reported in this paper.

Acknowledgments

This study was funded by the U.S. Department of Energy, Office of Energy Efficiency and Renewable Energy, Water Power Technologies Office under contract DE-AC05-76RL01830 at the Pacific Northwest National Laboratory (PNNL). The work was authored in part by the National Renewable Energy Laboratory (NREL), operated by Alliance for Sustainable Energy, LLC, for the U.S. Department of Energy (DOE) under Contract No. DE-AC36-08GO28308. Funding provided by U.S. Department of Energy Office of Energy Efficiency and Renewable Energy Water Power Technologies Office. All model simulations were performed using PNNL's Institutional Computing facility and NREL's Eagle Computing System. The views expressed in the article do not necessarily represent the views of the DOE or the U.S. Government. The U.S. Government retains and the publisher, by accepting the article for publication, acknowledges that the U.S. Government retains a nonexclusive, paid-up, irrevocable, worldwide license to publish or reproduce the published form of this work, or allow others to do so, for U.S. Government purposes.

References

[1] A.G. Borthwick, Marine renewable energy seascape, Engineering 2 (1) (2016) 69–78, http://dx.doi.org/10.1016/J.ENG.2016.01.011, URL: https://www.sciencedirect.com/science/article/pii/S2095809916301503.

[2] C.V. Weiss, R. Guanche, B. Ondiviela, O.F. Castellanos, J. Juanes, Marine renewable energy potential: A global perspective for offshore wind and wave exploitation, Energy Convers. Manage. 177 (2018) 43–54, http://dx.doi.org/10.1016/j.enconman.2018.09.059, URL: https://www.sciencedirect.com/science/article/pii/S0196890418310628.

[3] R.H. Karsten, J.M. McMillan, M.J. Lickley, R.D. Haynes, Assessment of tidal current energy in the minas passage, bay of fundy, Proc. Inst. Mech. Eng. A 222 (5) (2008) 493–507, http://dx.doi.org/10.1243/09576509JPE555.

[4] Z. Defne, K.A. Haas, H.M. Fritz, L. Jiang, S.P. French, X. Shi, B.T. Smith, V.S. Neary, K.M. Stewart, National geodatabase of tidal stream power resource in USA, Renew. Sustain. Energy Rev. 16 (5) (2012) 3326–3338, http://dx.doi.org/10.1016/j.rser.2012.02.061.

[5] D.R. Plew, C.L. Stevens, Numerical modelling of the effect of turbines on currents in a tidal channel - Tory Channel, New Zealand, Renew. Energy 57 (2013) 269–282, http://dx.doi.org/10.1016/j.renene.2013.02.001.

[6] S.P. Neill, M.R. Hashemi, M.J. Lewis, The role of tidal asymmetry in characterizing the tidal energy resource of Orkney, Renew. Energy 68 (2014) 337–350, http://dx.doi.org/10.1016/j.renene.2014.01.052.

[7] S.P. Neill, K.A. Haas, J. Thiébot, Z. Yang, A review of tidal energy—Resource, feedbacks, and environmental interactions, J. Renew. Sustain. Energy 13 (6) (2021) 062702, http://dx.doi.org/10.1063/5.0069452, arXiv:https://doi.org/10.1063/5.0069452.

[8] Z. Yang, T. Wang, R. Branch, Z. Xiao, M. Deb, Tidal stream energy resource characterization in the Salish Sea, Renew. Energy 172 (2021) 188–208, http://dx.doi.org/10.1016/j.renene.2021.03.028, URL: https://www.sciencedirect.com/science/article/pii/S0960148121003827.

[9] Z. Yang, T. Wang, Z. Xiao, L. Kilcher, K. Haas, H. Xue, X. Feng, Modeling assessment of tidal energy extraction in the western passage, J. Mar. Sci. Eng. 8 (6) (2020) http://dx.doi.org/10.3390/jmse8060411, URL: https://www.mdpi.com/2077-1312/8/6/411.

[10] IEC, Marine Energy—Wave, Tidal and Other Water Current Converters—Part 201: Tidal Energy Resource Assessment and Characterization: IEC TS 62600-201, International Electrotechnical Commission, Geneva, Switzerland, 2015.

[11] P.R. Spalart, Strategies for turbulence modelling and simulations, Int. J. Heat Fluid Flow 21 (3) (2000) 252–263.

[12] A.F. Shchepetkin, J.C. McWilliams, The regional oceanic modeling system (ROMS): a split-explicit, free-surface, topography-following-coordinate oceanic model, Ocean Model. 9 (4) (2005) 347–404.

[13] C. Chen, R.C. Beardsley, G. Cowles, J. Qi, Z. Lai, G. Gao, D. Stuebe, H. Liu, Q. Xu, P. Xue, J. Ge, S. Hu, R. Ji, R. Tian, H. Huang, L. Wu, H. Lin, Y. Sun, L. Zhao, An Unstructured Grid, Finite-Volume Community Ocean Model FVCOM User Manual (3rd Edition), Technical Report MITSG 12-25, Sea Grant College Program, Massachusetts Institute of Technology, 2013.

[14] K.M. Thyng, J.J. Riley, J. Thomson, Inference of turbulence parameters from a ROMS simulation using the k-ϵ closure scheme, Ocean Model. 72 (2013) 104–118, http://dx.doi.org/10.1016/j.ocemod.2013.08.008, URL: https://www.sciencedirect.com/science/article/pii/S1463500313001613.

[15] M. Guerra, R. Cienfuegos, J. Thomson, L. Suarez, Tidal energy resource characterization in Chacao Channel, Chile, Int. J. Mar. Energy 20 (2017) 1–16, http://dx.doi.org/10.1016/j.ijome.2017.11.002, URL: https://www.sciencedirect.com/science/article/pii/S2214166917300899.

[16] D.A. Brooks, The tidal-stream energy resource in Passamaquoddy–Cobscook Bays: A fresh look at an old story, Renew. Energy 31 (14) (2006) 2284–2295, http://dx.doi.org/10.1016/j.renene.2005.10.013, URL: https://www.sciencedirect.com/science/article/pii/S0960148105003289.

[17] B. Polagye, R. Bedard, System Level Design, Performance, Cost and Economic Assessment–Maine Western Passage Tidal In-Stream Power Plant, EPRI TP 006-ME, 2006.

[18] D. Xu, H. Xue, A numerical study of horizontal dispersion in a macro tidal basin, Ocean Dyn. 61 (2011) 623–637, http://dx.doi.org/10.1007/s10236-010-0371-6.

[19] T. Johnson, G.B. Zydlewski, Research for the sustainable development of tidal power in Maine, Maine Policy Rev. 21 (1) (2012) 58–65.

[20] C. Garrett, Tidal resonance in the Bay of Fundy and Gulf of Maine, Nature 238 (5365) (1972) 441–443.

[21] L. Kilcher, R. Thresher, H. Tinnesand, Marine Hydrokinetic Energy Site Identification and Ranking Methodology Part II: Tidal Energy, Technical Report NREL/TP-5000-66079, National Renewable Energy Lab.(NREL), Golden, CO (United States), 2016, http://dx.doi.org/10.2172/1330619.

[22] J.L. Best, Sediment transport and bed morphology at river channel confluences, Sedimentology 35 (3) (1988) 481–498, http://dx.doi.org/10.1111/j.1365-3091.1988.tb00999.x, URL: https://onlinelibrary.wiley.com/doi/abs/10.1111/j.1365-3091.1988.tb00999.x. arXiv:https://onlinelibrary.wiley.com/doi/pdf/10.1111/j.1365-3091.1988.tb00999.x.

[23] G. Constantinescu, S. Miyawaki, B. Rhoads, A. Sukhodolov, Numerical analysis of the effect of momentum ratio on the dynamics and sediment-entrainment capacity of coherent flow structures at a stream confluence, J. Geophys. Res.: Earth Surf. 117 (F4) (2012).

[24] G. Constantinescu, S. Miyawaki, B. Rhoads, A. Sukhodolov, Numerical evaluation of the effects of planform geometry and inflow conditions on flow, turbulence structure, and bed shear velocity at a stream confluence with a concordant bed, J. Geophys. Res.: Earth Surf. 119 (10) (2014) 2079–2097.

[25] A.N. Sukhodolov, J. Krick, T.A. Sukhodolova, Z. Cheng, B.L. Rhoads, G.S. Constantinescu, Turbulent flow structure at a discordant river confluence: Asymmetric jet dynamics with implications for channel morphology, J. Geophys. Res.: Earth Surf. 122 (6) (2017) 1278–1293.

[26] Z. Cheng, G. Constantinescu, Stratification effects on flow hydrodynamics and mixing at a confluence with a highly discordant bed and a relatively low velocity ratio, Water Resour. Res. 54 (7) (2018) 4537–4562.

[27] G.L. Mellor, T. Yamada, Development of a turbulence closure model for geophysical fluid problems, Rev. Geophys. 20 (4) (1982) 851–875, http://dx.doi.org/10.1029/RG020i004p00851, URL: https://agupubs.onlinelibrary.wiley.com/doi/abs/10.1029/RG020i004p00851. arXiv:https://agupubs.onlinelibrary.wiley.com/doi/pdf/10.1029/RG020i004p00851.

[28] L.H. Kantha, The length scale equation in turbulence models, Nonlinear Process. Geophys. 11 (1) (2004) 83–97, http://dx.doi.org/10.5194/npg-11-83-2004, URL: https://npg.copernicus.org/articles/11/83/2004/.

[29] G.L. Mellor, Users Guide for a Three Dimensional, Primitive Equation, Numerical Ocean Model, Program in Atmospheric and Oceanic Sciences, Princeton University, Princeton, NJ, 1998.

[30] S.M. Durski, S.M. Glenn, D.B. Haidvogel, Vertical mixing schemes in the coastal ocean: Comparison of the level 2.5 Mellor-Yamada scheme with an enhanced version of the K profile parameterization, J. Geophys. Res.: Oceans 109 (C1) (2004) http://dx.doi.org/10.1029/2002JC001702.

[31] G.R. Halliwell, Evaluation of vertical coordinate and vertical mixing algorithms in the HYbrid-Coordinate Ocean Model (HYCOM), Ocean Model. 7 (3) (2004) 285–322, http://dx.doi.org/10.1016/j.ocemod.2003.10.002.

[32] T. Kim, J.-H. Moon, Impact of improved Mellor–Yamada turbulence model on tropical cyclone-induced vertical mixing in the oceanic boundary layer, J. Mar. Sci. Eng. 8 (7) (2020) http://dx.doi.org/10.3390/jmse8070497, URL: https://www.mdpi.com/2077-1312/8/7/497.

[33] L. Kilcher, 2017 Western Passage Tidal Energy Resource Characterization Measurements, Technical Report, National Renewable Energy Lab.(NREL), Golden, CO (United States), 2017, http://dx.doi.org/10.15473/1635227.

[34] C. Amante, B.W. Eakins, ETOPO1 arc-minute global relief model: procedures, data sources and analysis, 2009.

[35] M. Love, K. Carignan1, B. Eakins, M. Sutherland, L. Beasley, S. McLean, Bathymetric digital elevation model of Eastern Canada: Procedures, data sources, and analysis, 2015, URL: https://www.ncei.noaa.gov/access/metadata/landing-page/bin/iso?id=gov.noaa.ngdc.mgg.dem:11503.

[36] C. Chen, J. Qi, C. Li, R.C. Beardsley, H. Lin, R. Walker, K. Gates, Complexity of the flooding/drying process in an estuarine tidal-creek salt-marsh system: An application of FVCOM, J. Geophys. Res.: Oceans 113 (C07052) (2008) http://dx.doi.org/10.1029/2007JC004328.

[37] Z. Xiao, Z. Yang, T. Wang, N. Sun, M. Wigmosta, D. Judi, Characterizing the non-linear interactions between tide, storm surge, and river flow in the Delaware Bay Estuary, United States, Front. Mar. Sci. 8 (2021) http://dx.doi.org/10.3389/fmars.2021.715557, URL: https://www.frontiersin.org/article/10.3389/fmars.2021.715557.

[38] B. Galperin, L. Kantha, S. Hassid, A. Rosati, A quasi-equilibrium turbulent energy model for geophysical flows, J. Atmos. Sci. 45 (1) (1988).

[39] S. Rao, H. Xue, M. Bao, S. Funke, Determining tidal turbine farm efficiency in the Western Passage using the disc actuator theory, Ocean Dyn. 66 (1) (2016) 41–57.

[40] J.T. Kelley, A.R. Kelley, Controls on surficial materials distribution in a rock-framed, glaciated, tidally dominated estuary: Cobscook Bay, Maine, Northeast. Nat. 11 (2004) 51–74, URL: http://www.jstor.org/stable/60225648.

[41] D.A. Brooks, Modeling tidal circulation and exchange in Cobscook Bay, Maine, Northeast. Nat. 11 (2004) 23–50, URL: http://www.jstor.org/stable/60225647.

[42] G.D. Egbert, S.Y. Erofeeva, Efficient inverse modeling of barotropic ocean tides, J. Atmos. Ocean. Technol. 19 (2) (2002) 183–204, http://dx.doi.org/10.1175/1520-0426(2002)019<0183:EIMOBO>2.0.CO;2.

[43] C.J. Willmott, On the validation of models, Phys. Geogr. 2 (2) (1981) 184–194, http://dx.doi.org/10.1080/02723646.1981.10642213, arXiv:https://doi.org/10.1080/02723646.1981.10642213.

[44] Z. Yang, T. Wang, A.E. Copping, Modeling tidal stream energy extraction and its effects on transport processes in a tidal channel and bay system using a three-dimensional coastal ocean model, Renew. Energy 50 (2013) 605–613, http://dx.doi.org/10.1016/j.renene.2012.07.024.

[45] J. Thiébot, N. Guillou, S. Guillou, A. Good, M. Lewis, Wake field study of tidal turbines under realistic flow conditions, Renew. Energy 151 (2020) 1196–1208, http://dx.doi.org/10.1016/j.renene.2019.11.129, URL: https://www.sciencedirect.com/science/article/pii/S0960148119318233.

[46] J. Thomson, B. Polagye, V. Durgesh, M.C. Richmond, Measurements of turbulence at two tidal energy sites in Puget Sound, WA, IEEE J. Ocean. Eng. 37 (3) (2012) 363–374, http://dx.doi.org/10.1109/JOE.2012.2191656.

[47] B. Gunawan, V.S. Neary, J. Colby, Tidal energy site resource assessment in the East River tidal strait, near Roosevelt Island, New York, New York, Renew. Energy 71 (2014) 509–517, http://dx.doi.org/10.1016/j.renene.2014.06.002, URL: https://www.sciencedirect.com/science/article/pii/S0960148114003425.

[48] S. Lee, M. Churchfield, P. Moriarty, J. Jonkman, J. Michalakes, Atmospheric and wake turbulence impacts on wind turbine fatigue loadings, in: 50th AIAA Aerospace Sciences Meeting Including the New Horizons Forum and Aerospace Exposition, 2012, http://dx.doi.org/10.2514/6.2012-540, URL: https://arc.aiaa.org/doi/abs/10.2514/6.2012-540. arXiv:https://arc.aiaa.org/doi/pdf/10.2514/6.2012-540.

[49] W.D. Lubitz, Impact of ambient turbulence on performance of a small wind turbine, Renew. Energy 61 (2014) 69–73, http://dx.doi.org/10.1016/j.renene.2012.08.015, URL: https://www.sciencedirect.com/science/article/pii/S0960148112004855. World Renewable Energy Congress – Sweden, 8–13 May, 2011, Linköping, Sweden.

[50] C.M. St. Martin, J.K. Lundquist, A. Clifton, G.S. Poulos, S.J. Schreck, Wind turbine power production and annual energy production depend on atmospheric stability and turbulence, Wind Energy Sci. 1 (2) (2016) 221–236, http://dx.doi.org/10.5194/wes-1-221-2016, URL: https://wes.copernicus.org/articles/1/221/2016/.

[51] H. Tennekes, J.L. Lumley, A First Course in Turbulence, The MIT Press, 1972, http://dx.doi.org/10.7551/mitpress/3014.001.0001.

[52] A.C.L. Bourgoin, S.S. Guillou, J. Thiébot, R. Ata, Turbulence characterization at a tidal energy site using large-eddy simulations: case of the alderney race, Phil. Trans. R. Soc. A 378 (2178) (2020) 20190499, http://dx.doi.org/10.1098/rsta.2019.0499, URL: https://royalsocietypublishing.org/doi/abs/10.1098/rsta.2019.0499. arXiv:https://royalsocietypublishing.org/doi/pdf/10.1098/rsta.2019.0499.

[53] P. Mercier, M. Grondeau, S. Guillou, J. Thiébot, E. Poizot, Numerical study of the turbulent eddies generated by the seabed roughness. Case study at a tidal power site, Appl. Ocean Res. 97 (2020) 102082.

[54] J. Thiébot, D.S. Coles, A.C. Bennis, N. Guillou, S. Neill, S. Guillou, M. Piggott, Numerical modelling of hydrodynamics and tidal energy extraction in the Alderney Race: a review, Philos. Trans. Ser. A Math. Phys. Eng. Sci. 378 (2178) (2020) 20190498, http://dx.doi.org/10.1098/rsta.2019.0498.

[55] A. Bourgoin, Bathymetry Induced Turbulence Modelling the Alderney Race Site: Regional Approach with TELEMAC-LES (Ph.D. thesis), Normandie Université, 2019.

[56] C. Argyropoulos, N. Markatos, Recent advances on the numerical modelling of turbulent flows, Appl. Math. Model. 39 (2) (2015) 693–732, http://dx.doi.org/10.1016/j.apm.2014.07.001, URL: https://www.sciencedirect.com/science/article/pii/S0307904X14003448.

[57] O.B. Fringer, C.N. Dawson, R. He, D.K. Ralston, Y.J. Zhang, The future of coastal and estuarine modeling: Findings from a workshop, Ocean Model. 143 (2019) 101458, http://dx.doi.org/10.1016/j.ocemod.2019.101458, URL: https://www.sciencedirect.com/science/article/pii/S1463500319301015.